

DTIC FILE COPY

Naval Research Laboratory

Washington, DC 20375-5000



3

NRL Memorandum Report 6233

AD-A200 617

**Determination of Ductile Alloy Constitutive
Response by Iterative Finite Element and
Laboratory Video Image Correlation**

P. MATIC, G. C. KIRBY III, AND M. I. JOLLES

*Mechanics of Materials Branch
Materials Science and Technology Division*

P. R. Father

*Geo-Centers, Inc.
Fort Washington, MD 20744*

August 9, 1988

DTIC
ELECTE
OCT 28 1988
S H D

88 1027 044

Approved for public release; distribution unlimited.

SECURITY CLASSIFICATION OF THIS PAGE

AD-A206 617

REPORT DOCUMENTATION PAGE				Form Approved OMB No 0704-0188													
1a REPORT SECURITY CLASSIFICATION UNCLASSIFIED			1b RESTRICTIVE MARKINGS														
2a SECURITY CLASSIFICATION AUTHORITY			3 DISTRIBUTION/AVAILABILITY OF REPORT														
2b DECLASSIFICATION/DOWNGRADING SCHEDULE			Approved for public release; distribution unlimited.														
4 PERFORMING ORGANIZATION REPORT NUMBER(S) NRL Memorandum Report 6233			5 MONITORING ORGANIZATION REPORT NUMBER(S)														
6a NAME OF PERFORMING ORGANIZATION Naval Research Laboratory		6b OFFICE SYMBOL (if applicable) Code 6382		7a NAME OF MONITORING ORGANIZATION													
6c ADDRESS (City, State, and ZIP Code) Washington, DC 20375-5000		7b ADDRESS (City, State, and ZIP Code)															
8a NAME OF FUNDING / SPONSORING ORGANIZATION Office of Naval Research		8b OFFICE SYMBOL (if applicable)		9 PROCUREMENT INSTRUMENT IDENTIFICATION NUMBER													
8c ADDRESS (City, State, and ZIP Code) Arlington, VA 22217		10 SOURCE OF FUNDING NUMBERS															
		PROGRAM ELEMENT NO 61153N22		PROJECT NO RR022- 01-48													
		TASK NO		WORK UNIT ACCESSION NO DN480-509													
11 TITLE (Include Security Classification) Determination of Ductile Alloy Constitutive Response by Iterative Finite Element and Laboratory Video Image Correlation																	
12 PERSONAL AUTHOR(S) Matic, P., Kirby, III, G.C., Father, P.R. and Jolles, M.I.																	
13a TYPE OF REPORT		13b TIME COVERED FROM _____ TO _____		14 DATE OF REPORT (Year, Month, Day) 1988 August 9													
				15 PAGE COUNT 63													
16 SUPPLEMENTARY NOTATION																	
17 COSATI CODES																	
<table border="1"><thead><tr><th>FIELD</th><th>GROUP</th><th>SUB-GROUP</th></tr></thead><tbody><tr><td></td><td></td><td></td></tr><tr><td></td><td></td><td></td></tr><tr><td></td><td></td><td></td></tr></tbody></table>						FIELD	GROUP	SUB-GROUP									
FIELD	GROUP	SUB-GROUP															
18 SUBJECT TERMS (Continue on reverse if necessary and identify by block number)																	
Constitutive Tensile necking																	
Finite element Cauchy stress-log strain																	
Video image Energy density																	
19 ABSTRACT (Continue on reverse if necessary and identify by block number)																	
<p>The accurate description of material response consists of a material constitutive formulation and material parameter values. The reduction of material test specimen load versus displacement data to constitutive parameters is often precluded by inelastic material response and deformation inhomogeneity within the specimen. For ductile engineering alloys, these effects are influenced by specimen geometry and must be uncoupled from specimen geometry to characterize the large strain material response. The accuracy of material parameters at such strains should be demonstrated for subsequent applications to design and analysis.</p> <p>Iterative solution for material constitutive parameters is discussed in the investigation. The use of video image processing of laboratory tensile test specimens is combined with successive computational simulations</p> <p style="text-align: right;">(Continues)</p>																	
20 DISTRIBUTION/AVAILABILITY OF ABSTRACT <input checked="" type="checkbox"/> UNCLASSIFIED/UNLIMITED <input type="checkbox"/> SAME AS RPT <input type="checkbox"/> DTIC USERS			21 ABSTRACT SECURITY CLASSIFICATION UNCLASSIFIED														
22a NAME OF RESPONSIBLE INDIVIDUAL Peter Matic			22b TELEPHONE (Include Area Code) (202) 767-5215		22c OFFICE SYMBOL Code 6382												

DD Form 1473, JUN 86

Previous editions are obsolete.

SECURITY CLASSIFICATION OF THIS PAGE

S/N 0102-LF-014-6603

19. ABSTRACTS (Continued)

of the specimen responses. The solution for HSLA-80 steel constitutive parameters, in the context of incremental plasticity theory, is presented. The material response is treated as the unknown in the computational simulations. It is iteratively modified to achieve correlation with the laboratory experiments. Two different specimen length-to-diameter aspect ratios are utilized to ensure the geometry independence of the material solution and to facilitate efficient solution. The constitutive iteration sequence illustrates the sensitivity of specimen response to material nonlinearity.

(RH) 4

CONTENTS

INTRODUCTION	1
CONSTITUTIVE PARAMETER SOLUTION METHODOLOGY	2
Tensile Specimen Phenomonology	2
Methodology Overview	4
Specimen Geometry for HSLA-80 Steel	6
Laboratory Hardware, Data Acquisition and Software	6
Computational Simulation Software	14
Comparison Software	19
Constitutive Parameter Determination Iterative Strategy	22
Results for HSLA-80 Alloy	24
SUMMARY	51
REFERENCES	51
APPENDIX I	55
APPENDIX II	57



Accession For	
NTIS GRA&I	<input checked="" type="checkbox"/>
DTIC TAB	<input type="checkbox"/>
Unannounced	<input type="checkbox"/>
Justification	
By _____	
Distribution/	
Availability Codes	
Dist	Avail and/or Special
A-1	

DETERMINATION OF DUCTILE ALLOY CONSTITUTIVE RESPONSE BY ITERATIVE FINITE ELEMENT AND LABORATORY VIDEO IMAGE CORRELATION

INTRODUCTION

Material constitutive theories are developed to predict the continuum response of materials to applied stress and strain histories. A particular theory consists of a mathematical formulation and a set of material constitutive parameters. The former is traditionally developed to describe a particular class of materials, the latter a particular material within the class. From practical and economical considerations it is desirable to obtain the numerical values for a small number of material constitutive parameters, appearing in the formulation, from a small number of simple laboratory material test specimens. Proof of parameter applicability over the observed range of deformation should be demonstrated.

Constitutive parameters are ideally determined from macroscopically homogeneous states of deformation. Material specimens designed for this purpose include standard uniaxial tension (ASTM, 1984b) and torsion (ASTM, 1984a) specimens and various approaches to biaxial testing (e.g. Krempl and Lu, 1984, and McDowell, 1987). Global load and displacement data may be directly normalized to local stress and strain parameter values in the range of specimen deformation which satisfies the homogeneity and proportionality of the specimen deformation.

For ductile structural alloys, only the initial portion of the specimen deformation history satisfies the deformation homogeneity requirement. Inhomogeneous multiaxial deformation is present over most of the specimen deformation history. Large scale deformation localization, such as tensile specimen necking (e.g. Bridgman, 1952), preclude the transition from initial homogeneous, small strain deformations to homogeneous, large strain deformations. Deformation localization at small scales comparable to the material microstructure may also occur in some materials. This further disrupts the original deformation field in the form of slip bands (e.g. Hartley, Duffy, and Rawley, 1987). The result common to both localization modes is the loss of specimen deformation homogeneity. Data reduction techniques which depend on deformation homogeneity cease to be valid under these circumstances. For many engineering alloys the upper limit of homogeneous deformation lies in the range of 10^{-2} to 10^{-1} strain. Phenomenological features common to inelastic, path dependent material behavior are inevitably present, beyond this limit, in material test specimens subjected to sufficient deformation magnitudes.

For engineering alloys, strains of 10^0 are not uncommon prior to material fracture. The difference between the strain corresponding to the limits of deformation homogeneity and the strains encountered prior to failure represent a considerable portion of the material's response. The importance of accurate constitutive parameter values to describe this range of deformation is apparent for applications encompassing material damage, fracture and processing. The use of a local fracture criterion, within the broad class of material damage theory (as reviewed by Kracinovic, 1984 and Kachanov, 1986), offers the advantage of thermodynamic consistency and scale insensitivity for the prediction of engineering alloy response if accurate material parameter values are available.

Investigations of material constitutive response in the traditional domain of homogeneous specimen deformation may be divided into two main groups: (i) multiaxial small deformation at low deformation rates (e.g. Naghdi and Nikkel, 1986) and (ii) uniaxial large deformation at high deformation rates (e.g. Klepaczko and Chiem, 1986). Considerable insight into material response has been obtained from these domains of investigation. For geometrically nonlinear problems involving large strains, arbitrary multiaxial deformation histories and deformation rate sensitivity, however, it is necessary to develop methods which utilize the full range of test specimen response in order to accurately describe the full range of material response.

The purpose of this investigation is to enhance methods which uncouple the effects of specimen geometry, dominated by large scale deformation localization in material test specimens, from the material continuum response. The material constitutive parameters, complementing an inelastic constitutive formulation, are treated as the unknown quantities. Iterative solution for the material constitutive parameters is achieved through successive computational simulations of laboratory tensile specimen experiments. Load histories and surface displacements obtained by video image processing of the laboratory experiments are compared to computational predictions. These comparisons are then used to guide the iterative solution process and assess the material response internal to the specimen. The methods discussed are employed for the constitutive characterization of HSLA-80 steel.

CONSTITUTIVE PARAMETER SOLUTION METHODOLOGY

Tensile Specimen Phenomenology

For a material which exhibits significant ductility, specimen deformation will produce deformation localization, in the form of necking, in the test section. For mathematically small strains, encountered prior to and immediately beyond specimen yield, the uniaxial Cauchy stress-logarithmic strain curve, i.e. $\sigma - \epsilon$, for the material is approximately equal to the standard engineering stress-engineering strain curve, i.e. $\bar{\sigma} - \bar{\epsilon}$, obtained from normalized global specimen load-displacement data. For strains which are mathematically large, but encountered prior to the onset of specimen necking, global specimen load-displacement responses can still be normalized to approximate the Cauchy stress-log strain curve. Following this point in the specimen deformation history, the deformation within the test section can no longer be approximated as uniform. Other methods must be employed to determine the $\sigma - \epsilon$ response of the material. High strength, low alloy (HSLA) steel specimens exhibit this type of response.

The mechanics of necking itself has received considerable attention (e.g. Hutchinson, 1979). A variety of analytical and computational approaches to tensile specimen phenomenology exist. They are briefly reviewed here to introduce the approach used for material parameter characterization in this investigation.

Analytical approaches to the necking problem have been developed to describe the global specimen load-displacement response for different power law hardening material models and parameter values. The influence of material parameters on the growth of initial inhomogeneities in the specimen gage section was examined by Hart (1967) and Ghosh (1974). The distinct influence of initial versus material prestrain inhomogeneities on specimen instability has been considered by Jonas, Holt and Coleman (1976), Ghosh (1977) and Lin, Hirth and Hart (1981). Kocks, Jonas and Mecking (1979) expressed the specimen material behavior in terms of state parameters to reexamine the specimen neck growth behavior.

Additional work by Jonas and Baudelet (1977) incorporated distributed crack and distributed void cavity generation and growth features into the specimen material model. G'Sell and Jonas

(1979), G'Sell, Aly-Helal and Jonas (1983) and Hutchinson and Neale (1983) examined the features of polymer necking in the context of the global uniaxial approach to inhomogeneity growth and specimen stability. Recently, Lian and Baudelet (1986) developed a correlation between uniaxial elongation to failure, strain rate sensitivity and strain hardening.

Computational methods have been used extensively to examine the three-dimensional aspects of the necking phenomenon. Chen (1971) applied the Kantorovich method and Chen (1983) applied finite difference techniques to the problem of necking in tapered specimens. Early finite element approaches utilizing a bifurcation criteria to initiate tensile specimen necking were considered by Needleman (1972).

Finite element methods have been developed to include defects of a size significantly below the continuum scale, modeled as void densities and incorporated into three dimensional constitutive damage formulations by Perzyna (1984) for necking and localization studies, Tvergaard and Needleman (1984) on nucleation and growth effects, Kleiber (1986) on bifurcation and localization, and Needleman and Becker (1986) and Tvergaard (1987) on the influence of yield surface curvature.

Shear localization has also received attention, and is mentioned here, although this mode of deformation lies outside the scope of this investigation. Recent computational and experimental effort in this area includes Tvergaard, Needleman and Lo (1981) on plane strain tensile localization, Triantafyllidis, Needleman and Tvergaard (1982) on shear bands in pure bending, Semiatin, Staker and Jonas (1984) on rate effects and Korbel, Raghunathan, Teirlinck, Spitzig, Richmond and Embury (1984) on the influence of hydrostatic pressure on shear banding.

The investigations discussed above attribute the onset and subsequent development of tensile specimen necking to either (i) global instability of deformation predicted by uniaxial formulations, (ii) the presence of specimen geometry imperfections, in the form of specimen taper, or mechanical imperfections, in the form of prestrained zones at the desired neck location, or (iii) material instability criteria which serve to localize deformation. Material constitutive parameters, however, are typically obtained from specimen data prior to necking for use in the analysis of the necking phenomenon. In a practical sense, this defeats the purpose of the tensile specimen as a means by which to obtain constitutive parameters valid over the full range of material deformation.

The general problem of constitutive parameter solution from computational modeling of material test specimens was discussed by Pister (1974). Application to plane stress deformation of nonlinear elastic solids was considered by Iding, Pister and Taylor (1974). The constitutive parameter problem for inelastic solids was addressed by Norris, Scudder and Quinones (1978) through the development of a uniaxial true stress-true strain relationship from finite difference simulation of the tensile specimen gage length. Successive iterations on the true stress-true strain relationship were successful at correlating predicted specimen response with laboratory specimen data. The computational model, however, invoked a linear specimen taper to initiate specimen necking at the center of the specimen.

Recent investigations by Matic (1985) and Matic, Kirby and Jolles (1987) treated the uniaxial material Cauchy stress-log strain curve of HY-100 steel as the unknown parameter in a series of iterative finite element simulations of defect free specimens. Single and multiple geometry tensile specimen responses, respectively, were considered. Multiple geometries were achieved through different length-to-diameter specimen gage aspect ratios (L_0/D_0). After each simulation, the predicted specimen response was compared to the associated laboratory specimen response. When satisfactory agreement was reached between predicted and observed specimen responses, the solution curve and associated parameters were adopted for the material response.

The results of these studies demonstrated that tensile specimen necking is a consequence of the natural interaction between specimen geometry, applied load and the material stress-strain curve non-linearity. The relatively simple rate independent, isothermal incremental plasticity formulation successfully used for these analyses (and reviewed below) also suggest that certain features of tensile specimen deformation may be described without the use of the more complicated formulations mentioned previously. The determination of accurate constitutive parameters for a particular constitutive formulation must be given consideration equal to that given the choice of the formulation itself. This is particularly true if the consistent and accurate prediction of material response is possible with a simpler formulation.

The solution strategy developed for the determination of HY-100 constitutive parameters, as discussed by Matic, Kirby and Jolles (1987), was based on the correlation of experimentally observed and computationally predicted engineering stress-engineering strain response derived from global load-displacement results. The iterative solution of the material constitutive parameters, in the form of the Cauchy stress-log strain curve, was obtained by computational simulations of four different specimen geometries tested in the laboratory. The following points relevant to iterative solution strategy were observed:

- (1) Lower L_0/D_0 specimens provide a good gross indication of the material Cauchy stress-log strain curve. A larger relative portion of the specimen gage volume sustains monotonically increasing deformation as part of the necking process.
- (2) Higher L_0/D_0 specimens are most useful to guide minor adjustments to the curve obtained from the low L_0/D_0 specimen data. A smaller portion of the higher L_0/D_0 specimen is involved in the actively yielding neck in the specimen. As a result, the balance between values of stress, strain and tangent modulus and the relative tendency for the neck to continue deforming while the remainder of the specimen unloads is addressed.
- (3) Translation of the material Cauchy stress-log stress curve in the stress axis direction results in a comparable translation of the predicted nominal stress-nominal strain curve.
- (4) Expansion of the material Cauchy stress-log strain curve in the strain axis direction, corresponding to the deformation subsequent to the peak engineering stress, tends to accelerate the advanced stages of necking.

These guidelines were effective for obtaining the solution curve for HY-100 steel and significant insight into the tensile specimen phenomenology. A more quantitative strategy for solution is desirable for rate independent materials, and even necessary for extension and formalization of this process to rate and temperature dependent materials. Means of identifying the location of spatial deformation errors and the onset of constitutive parameter errors which govern the path dependent deformation are necessary to guide the iterative solution. Current developments in computational technology are relevant for both the analytical and experimental portions of the constitutive parameter solution procedure.

Methodology Overview

The constitutive parameter solution procedure developed in this investigation employs iterative computational simulation of laboratory experiments to solve for the inelastic material constitutive response in the form of Cauchy stress-logarithmic strain pairs. These stress-strain pairs describe a multilinear curve representing the nonlinear uniaxial response of the material. The solution procedure (Figure 1) establishes agreement between laboratory experiment and computational simulation of the

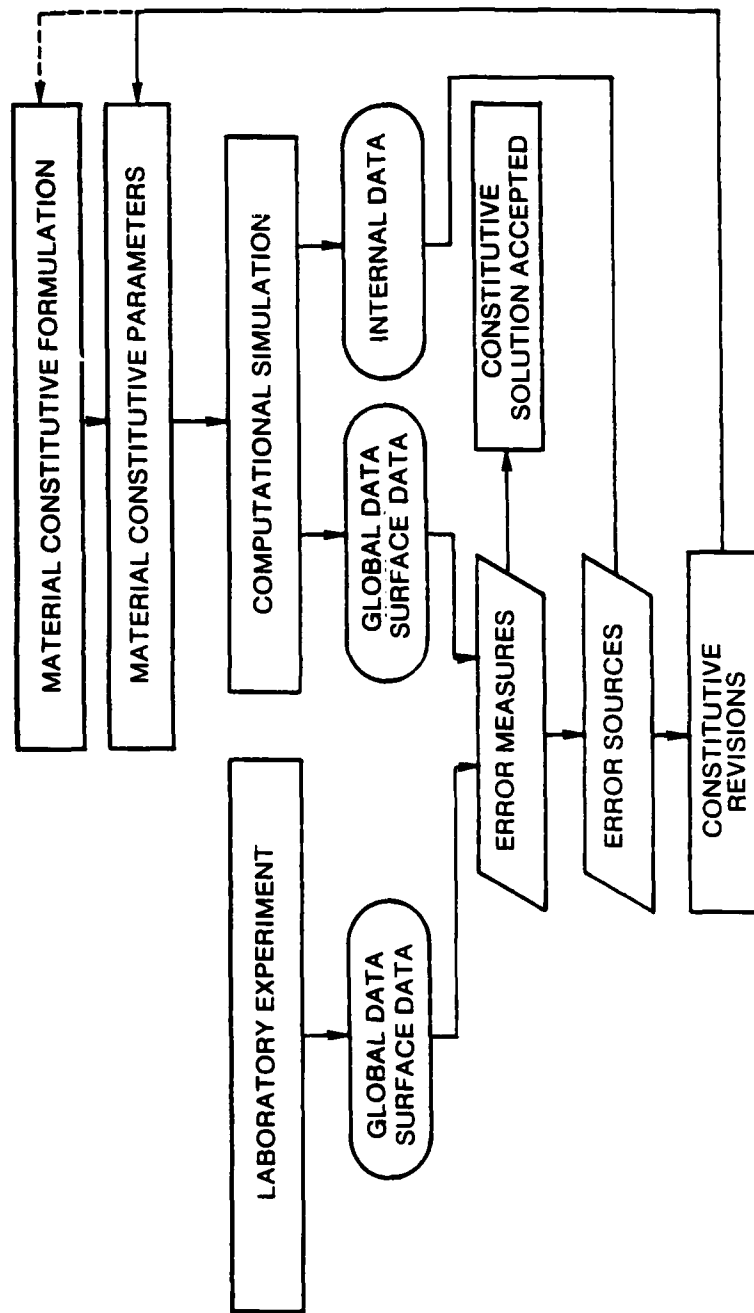


Figure 1—Constitutive parameter solution flow chart.

specimen. This is expressed in terms of the global load-displacement responses of the specimen, normalized to engineering stress-engineering strain. Divergence of the two curves indicates that significant constitutive response errors remain within the computational simulation of the specimen gage volume and another iteration is warranted.

A finite number of points on the laboratory and computational specimen profile are used to define smaller gage volumes within the specimen gage volume. These smaller gage volumes will be referred to as subgage volumes for this discussion. Laboratory and computational subgage axial stretch ratios were compared to identify the locations of relative differences and agreement between predicted and observed subgage responses. This information was in turn used to identify necessary changes in the current constitutive parameter iteration for the next computational simulation. The number of points was selected to reflect a balance between resolution errors of adjacent points in the laboratory profile and subgage length-to-diameter aspect ratios (which maintain a balance between material volume and projected surface aspect ratio). Subgage surface axial stretch ratios were calculated from both laboratory and computational data.

Significant differences in computational predictions and laboratory measurements of subgage axial stretch ratios suggest the location of predicted material deformation within the specimen gage which is not representative of the material behavior in the laboratory. The computationally predicted material response within the subgage volume in question was used to identify the constitutive parameters range producing the predicted specimen error. The Cauchy stress-log strain pairs which define the constitutive parameter range in question are identified and modified for subsequent iteration.

The parameters for the HSLA-80 steel alloy were obtained using this strategy and demonstrate its implementation. The following description of the HSLA alloy characterization is divided into sections describing specimen geometry, laboratory experiments, computational simulations, data comparison and constitutive parameter iteration.

Specimen Geometry for HSLA-80 Steel

Four different HSLA-80 cylindrical tensile specimen geometries were tested in the laboratory. A sufficient range of global specimen responses is necessary to facilitate the solution of geometry independent material constitutive parameters. This range is, generally speaking, not known a priori. For this investigation, specimen length-to-diameter, i.e. L_0/D_0 , ratios of 1.0, 2.0, 3.0 and 4.0 were obtained from a single specimen diameter of 1.27 cm (0.50") and cylindrical gage lengths of 1.27 cm (0.50"), 2.54 cm (1.00"), 3.81 cm (1.50") and 5.08 cm (2.00"). These will be referred to as Specimen No. 1 through Specimen No. 4, respectively, and are shown in Figure 2. The range of L_0/D_0 values was selected on the basis of previous investigations into the geometry dependence of cylindrical tensile specimen global load versus displacement response for HY-100 steel. The range of global specimen responses produced by the different HSLA specimen geometries, presented below, was sufficiently large so that computational simulation of two geometries was sufficient to ensure geometry independence of the solution constitutive parameters. The two lower aspect ratio specimens (i.e. Specimens No. 1 and 2) were selected to minimize computational model size.

Laboratory Hardware, Data Acquisition and Software

The first step in the solution procedure was the laboratory testing of the tensile specimens. Five specimens were tested for each geometry. Measurements of the specimen diameter along each specimen gage section were made prior to testing and are tabulated in Appendix I. The specimens were spray painted flat black. White gage marks were painted on the specimen at the ends of the gage length. A white background was placed behind the specimen. The resulting contrast was sufficient to

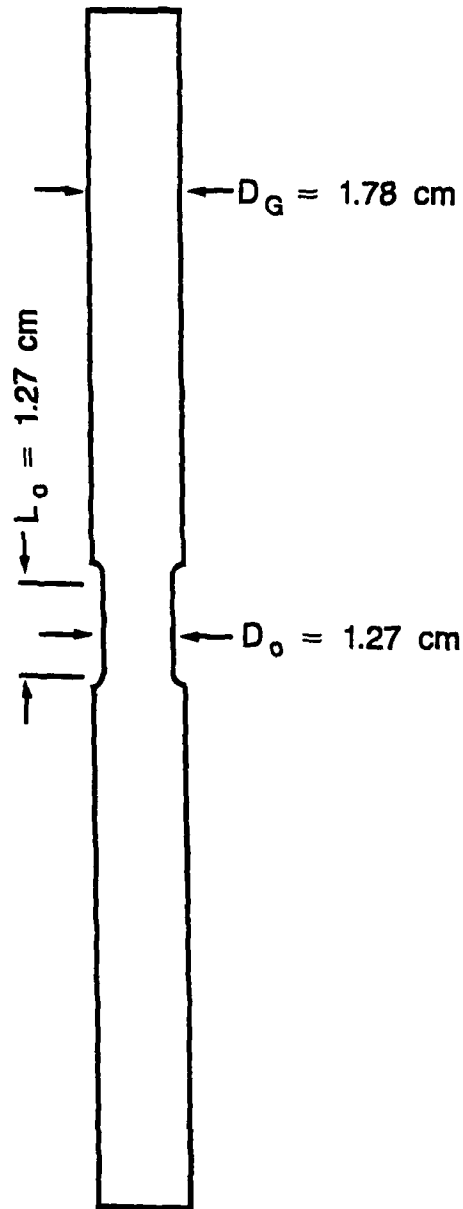


Figure 2 — Cylindrical tensile specimen geometries, (a) Specimen No. 1, $L_0 = 1.27 \text{ cm}$, $D_0 = 1.27 \text{ cm}$, (b) Specimen No. 2, $L_0 = 2.54 \text{ cm}$, $D = 1.27 \text{ cm}$, (c) Specimen No. 3, $L_0 = 3.81 \text{ cm}$, $D_0 = 1.27 \text{ cm}$, and (d) Specimen No. 4, $L_0 = 5.08 \text{ cm}$, $D_0 = 1.27 \text{ cm}$.

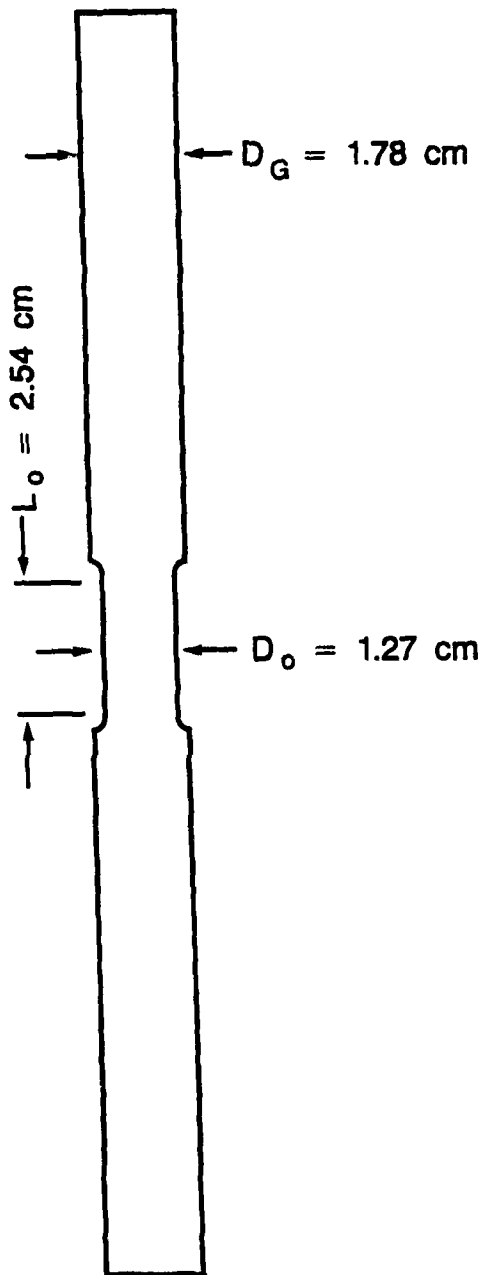


Figure 2 (Continued) — Cylindrical tensile specimen geometries, (a) Specimen No. 1, $L_0 = 1.27$ cm, $D_0 = 1.27$ cm, (b) Specimen No. 2, $L_0 = 2.54$ cm, $D_0 = 1.27$ cm, (c) Specimen No. 3, $L_0 = 3.81$ cm, $D_0 = 1.27$ cm, and (d) Specimen No. 4, $L_0 = 5.08$ cm, $D_0 = 1.27$ cm.

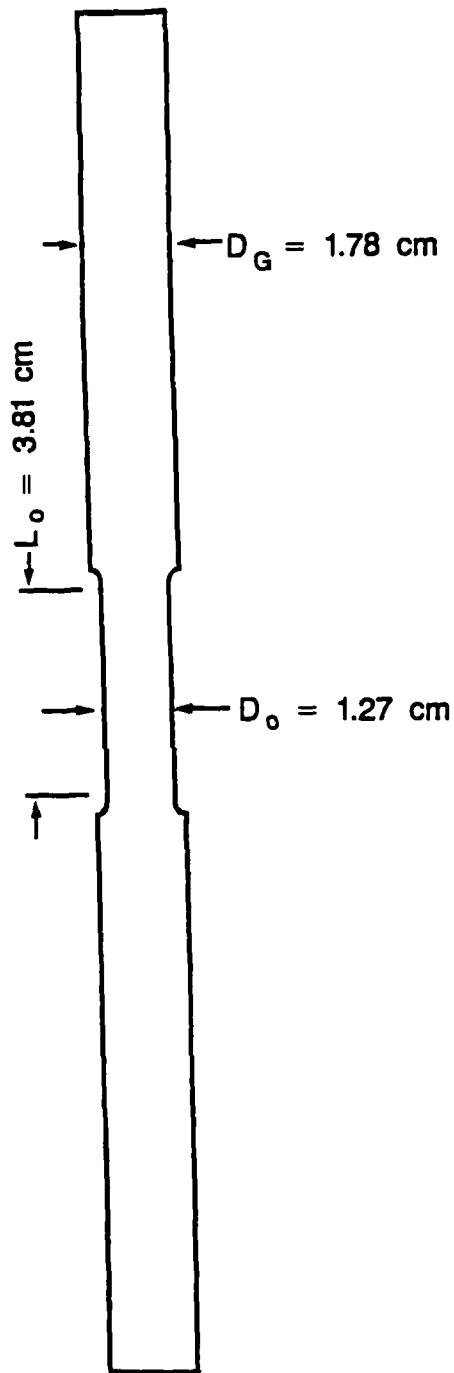


Figure 2 (Continued) — Cylindrical tensile specimen geometries, (a) Specimen No. 1, $L_0 = 1.27 \text{ cm}$, $D_0 = 1.27 \text{ cm}$, (b) Specimen No. 2, $L_0 = 2.54 \text{ cm}$, $D = 1.27 \text{ cm}$, (c) Specimen No. 3, $L_0 = 3.81 \text{ cm}$, $D_0 = 1.27 \text{ cm}$, and (d) Specimen No. 4, $L_0 = 5.08 \text{ cm}$, $D_0 = 1.27 \text{ cm}$.

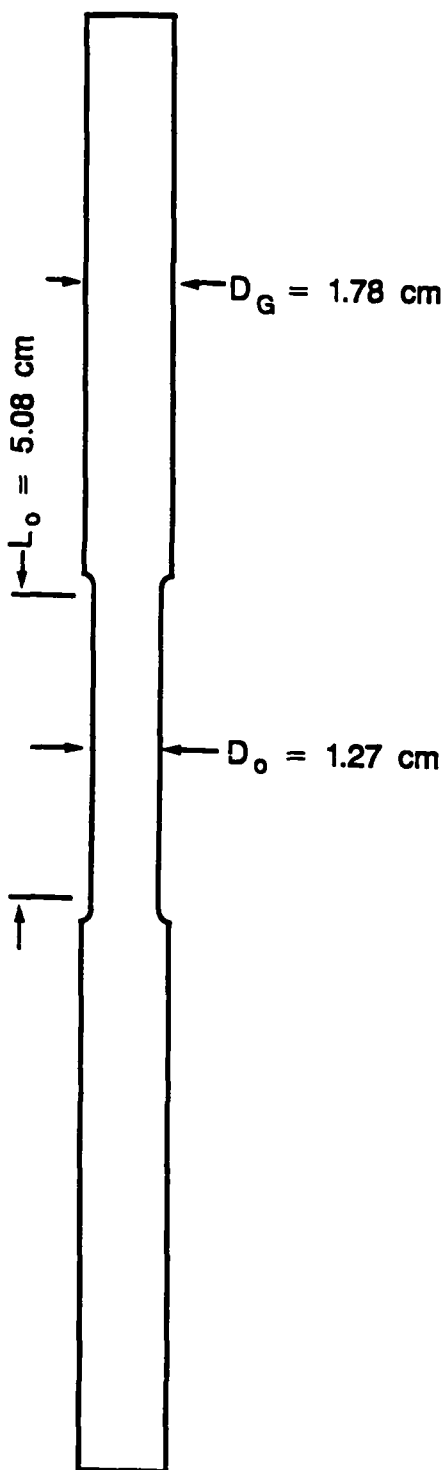


Figure 2 (Continued) — Cylindrical tensile specimen geometries, (a) Specimen No. 1, $L_0 = 1.27$ cm, $D_0 = 1.27$ cm, (b) Specimen No. 2, $L_0 = 2.54$ cm, $D = 1.27$ cm, (c) Specimen No. 3, $L_0 = 3.81$ cm, $D_0 = 1.27$ cm, and (d) Specimen No. 4, $L_0 = 5.08$ cm, $D_0 = 1.27$ cm.

clearly define the specimen edges for video recording during the test and subsequent digital image analysis. The effect of specimen geometry on the global load-displacement responses, normalized to engineering stress-engineering strain, was evident beyond strains of 0.10 (Figure 3). No significant variation in the engineering stress-engineering strain behavior was observed for specimens of the same geometry.

Testing was performed in a closed loop servohydraulic testing machine under displacement control at a rate of 0.107 cm/minute (0.042 inch/minute). A load cell provided an analog voltage that was proportional to the load. The load signal was digitized for recording by a microcomputer at 10 second intervals.

The microcomputer was equipped with a video digitizing board. The board was capable of sequentially storing and displaying one video frame. The resolution of the board was 384 pixels horizontally by 512 pixels vertically by 8 bits per pixel. The average light intensity over the area of each pixel was assigned a numerical value between 0 and 255 with black equal to zero and white equal to 255. The video memory was fully transparent to the central processing unit for rapid manipulation of pixels. The video input to the board was provided by a charge coupled device (CCD) camera. The output of the video board was fed to a video cassette recorder (VCR) and a video monitor.

The microcomputer started the testing machine, controlled the video digitizing board, performed data acquisition and terminated the experiment. After each 10 second time interval the specimen image was frozen. Software was developed to write the load and gage mark separation to the video memory. Still images of the specimen were recorded by the VCR for subsequent analysis of the specimen profile. Data written to the disk file included elapsed time, load, actuator displacement and the position of the top and bottom gage marks.

The position of the gage marks was defined to be the center of the white gage marks painted on the specimen. The center of the gage marks were located by the video image program in the following manner. Two points along the longitudinal axis of the specimen, above and below the specimen gage section, were interactively selected by the user. The histogram of the grey levels between these two points was calculated. The histogram was bimodal since the white gage marks lay on a black background. Bimodal peaks were identified and a threshold value based upon the weighted average of the bimodal peaks was determined. Pixels with grey levels greater than the threshold were assumed to define the gage mark thickness. Gage mark edges were determined from the black-white transition. Gage mark center coordinates were defined as the edge coordinate average. The engineering strain was determined using the gage mark separation. The experimental error was less than 0.3 percent, depending upon magnification.

Coordinates of the left and right specimen edges, defining the specimen profile, were obtained at evenly spaced intervals along the edge. The procedure is shown schematically in Figure 4. For the HSLA-80 experiments considered here, ten specimen profiles per test were selected from the total number of stored video images which covered the total test time by equal time intervals. User input consisted of (i) numerical values of the elapsed time and load and (ii) cursor positions on the recalled video image defining the two gage marks and (iii) five additional points between the gage marks used to define the specimen profile left and right edges. A cubic spline was fit through these points, superimposed on the actual edge and visually observed on the video monitor. Based on the spline fit for the left and right edges, the minimum diameter of the specimen was determined and its location displayed on the image. The process was interactive so that in the event of an error in cubic spline implementation the process may be repeated on command of the user.

Acceptance of the profile edges and minimum diameter is followed by user selection of the number of vertical intervals into which the profile is to be segmented. Elapsed time, load, diameters

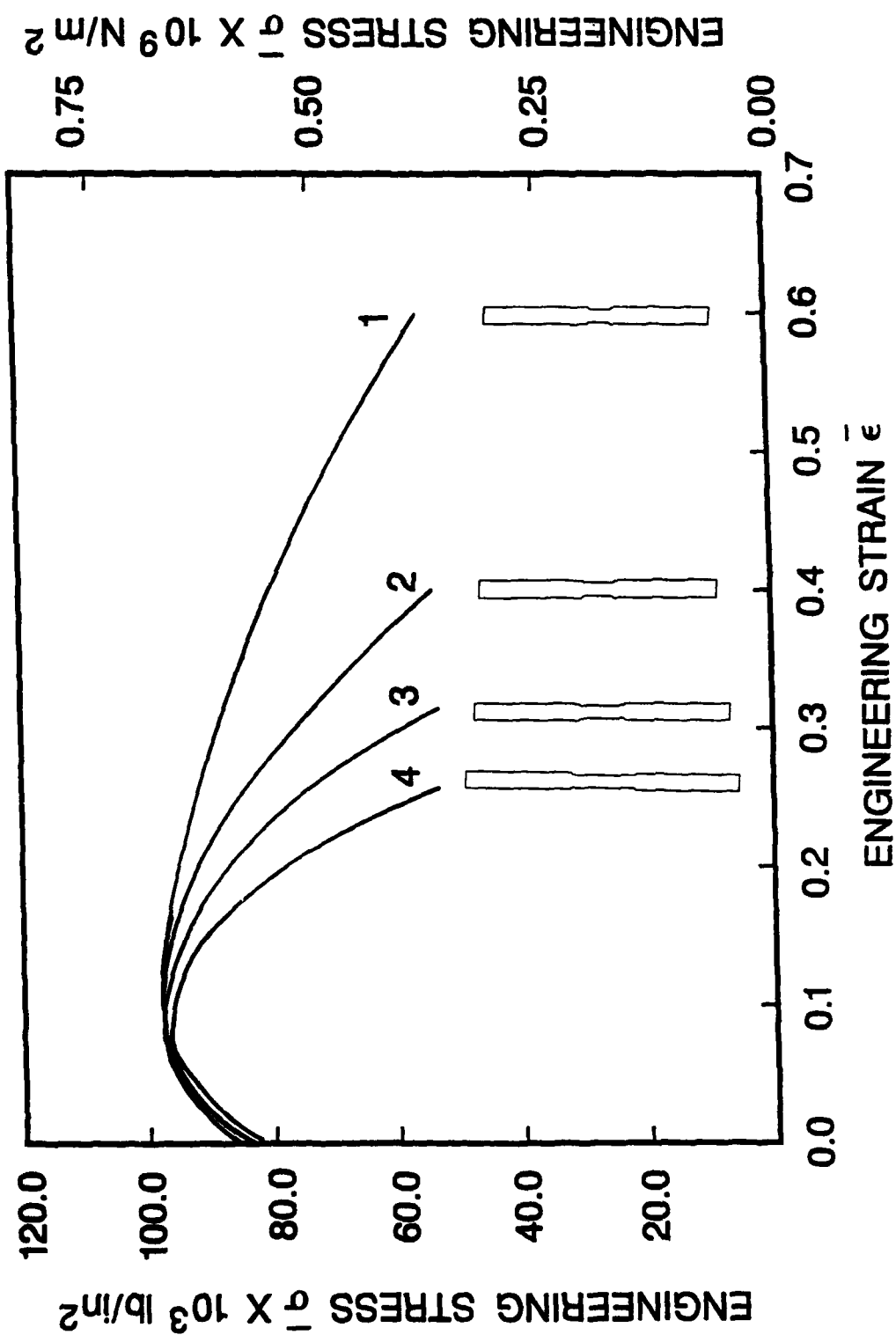


Figure 3—Engineering $\bar{\sigma}$ — $\bar{\epsilon}$ curves for HSLA-80 steel specimens calculated from experimental load and displacement data.

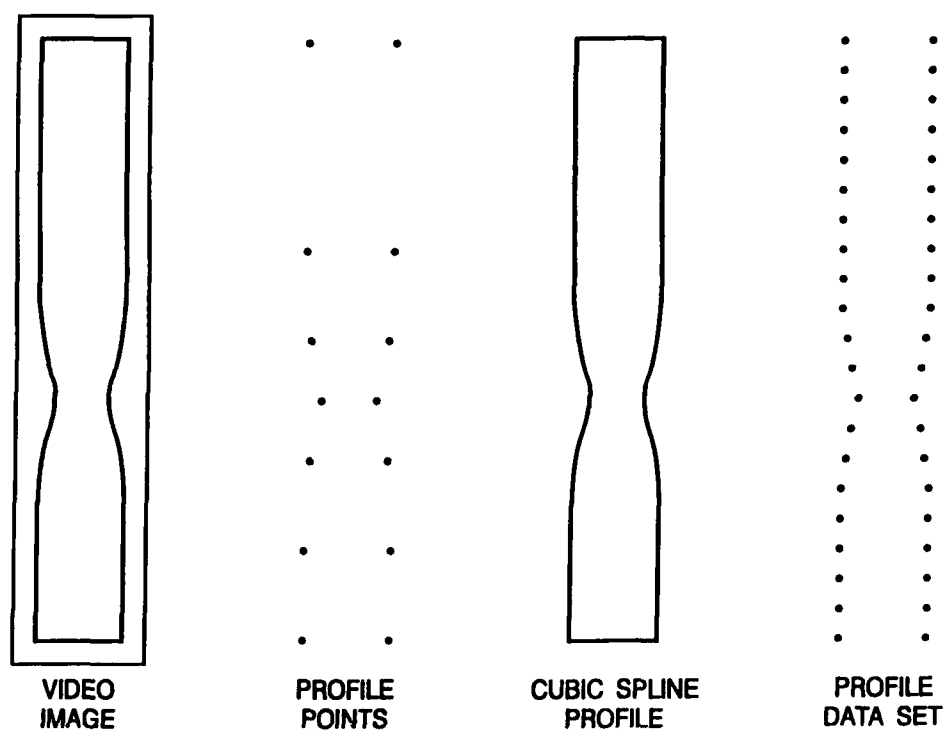


Figure 4—Laboratory software schematic diagram.

and corresponding longitudinal coordinates are written to a data file for subsequent use in comparing experimental and computational data. Errors associated with the diameter and corresponding longitudinal coordinate measurement are also dependent upon magnification. The largest errors were encountered for the high L_0/D_0 aspect ratio specimens. For this specimen geometry, the horizontal resolution was 0.0318 cm/pixel (0.0125 inch/pixel) and the vertical resolution was 0.0178 cm/pixel (0.007 inch/pixel). The smallest errors were encountered for the low L_0/D_0 aspect ratio specimens. In this case, vertical and horizontal resolutions were 0.0127 cm/pixel (0.005 inch/pixel) and 0.0076 cm/pixel (0.003 inch/pixel) respectively.

Computational Simulation Software

The second step in the constitutive parameter solution procedure was iterative computational simulation of the laboratory tensile specimens. The ABAQUS (Version 4.5) finite element code (Hibbitt et al., 1984b) was used for the computational simulations. Finite element models for the two lower aspect ratio specimens are shown in Figure 5. Axisymmetry of the specimen required that only one quarter of the specimen diameter cross section be modeled.

Type CAX8H axisymmetric elements were used. These were 8-noded elements with quadratic displacement interpolation and an independently interpolated linear hydrostatic stress. The hydrostatic stress was coupled to the constitutive relation using a Lagrange multiplier. The use of these hybrid elements prevented physically unrealistic displacement constraints from propagating through the grid. Such constraints can lead to artificially "stiff" responses of standard elements for incompressible or nearly incompressible deformation.

All analyses were performed with full geometric nonlinearity to account for large strains and large rotations. An updated Lagrangian formulation was used for incremental solutions in ABAQUS. A modified Rik's algorithm, being load and displacement controlled, was used to ensure numerical stability since the specimen axial load was known to decrease for large specimen elongation.

Displacement boundary conditions were prescribed to simulate the physical loading conditions of the laboratory tests. A 7.62 cm (3.0 inch) wide strip on the lateral surface of the grip section of each specimen was subjected to uniform axial displacements. The boundary conditions reproduced, for computation, the physical nature of the loads applied by the hydraulic grips.

An incremental rate independent plasticity theory was used for the material constitutive model (Hibbitt et al., 1984b). Total strains in the multiaxial strain state ϵ_{ij} were obtained by the integration of the linearly decomposed rate of deformation tensor D_{ij} . This integration was performed under the assumption that the elastic strains remain infinitesimal, as is the case in this investigation. The total multiaxial strain state ϵ_{ij} , expressed in terms of elastic and plastic components, was

$$\epsilon_{ij} = \epsilon_{ij}^e + \epsilon_{ij}^p \quad (1)$$

The total logarithmic uniaxial strain ϵ , consistent with the integration of the rate of deformation tensor for a multiaxial strain state, was decomposed as

$$\epsilon = \epsilon^e + \epsilon^p \quad (2)$$

The yield function f takes the form

$$f(\tau_{ij}) = \tau(\epsilon^p) \quad (3)$$

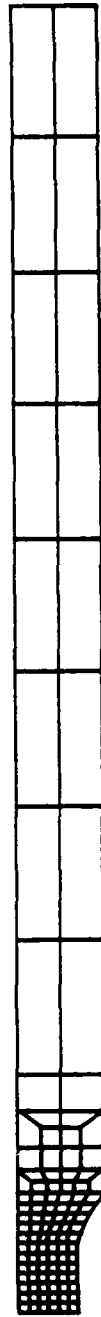


Figure 5 — Axisymmetric finite element models for computational simulation, (a) Specimen No. 1, $L_0 = 1.27$ cm, $D_0 = 1.27$ cm, and (b) Specimen No. 2, $L_0 = 2.54$ cm, $D_0 = 1.27$ cm.

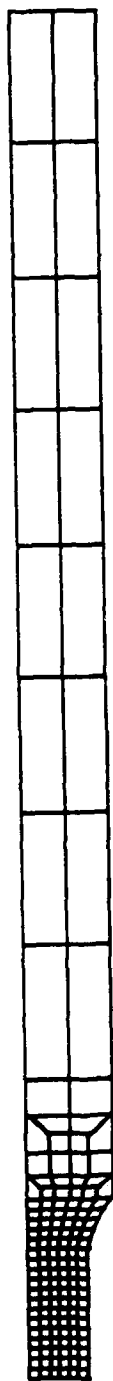


Figure 5 (Continued) — Axisymmetric finite element models for computational simulation, (a) Specimen No. 1, $L_0 = 1.27$ cm, $D_0 = 1.27$ cm, and (b) Specimen No. 2, $L_0 = 2.54$ cm, $D_0 = 1.27$ cm.

where τ_{ij} and τ are the multiaxial and uniaxial Kirchoff (or Trefftz) stress states, respectively. The associated flow rule governed plastic strain increments by the relation

$$d\epsilon_{ij}^p = \lambda \frac{\partial f}{\partial \tau_{ij}} \quad (4)$$

In the case of purely elastic behavior $\lambda = 0$. For active material yielding,

$$\lambda = d\epsilon^p \frac{\tau}{\left[\tau_{ij} \frac{\partial f}{\partial \tau_{ij}} \right]} \quad (5)$$

$$\lambda > 0 \quad (6)$$

Plastic strain increments also satisfied a dissipation equivalence condition

$$\tau d\epsilon^p = \tau_{ij} d\epsilon_{ij}^p \quad (7)$$

and a consistency condition

$$\frac{\partial f}{\partial \tau_{ij}} d\tau_{ij} - \frac{\partial \tau}{\partial \epsilon^p} d\epsilon^p = 0 \quad (8)$$

The von Mises yield function

$$f(\tau_{ij}) = \frac{3}{2} (s_{ij} s_{ij})^{1/2} \quad (9)$$

was employed. The deviatoric stress tensor s_{ij} was defined as

$$s_{ij} = \tau_{ij} - \frac{1}{3} t_{kk} s_{ij} \quad (10)$$

where the hydrostatic component of stress is $\tau_{kk}/3$.

The Kirchoff stress and logarithmic strain measures are employed because of the advantages gained in computational implementation. The Kirchoff stress tensor τ_{ij} is approximately equal to the more physically motivated Cauchy stress tensor σ_{ij} for deformations involving only small changes in volume. This condition was implicit in these analyses. The uniaxial Cauchy stress-log strain constitutive response of the material was formally input, in multilinear form, as Cauchy stress and logarithmic strain pairs for the ABAQUS program.

Software was developed to translate the ABAQUS results into a format compatible with the data comparison subroutine which reads the computational and experimental results. A subroutine was linked to the ABAQUS library to scan the appropriate ABAQUS data file for relevant data. The subroutine performed two tasks. First, bulk data was translated into sequential files respective of each increment encountered. Second, overall file size was reduced to include only those quantities requested by the user to generate surface displacement (Figure 6), axial load and constitutive data for specified solution increments.

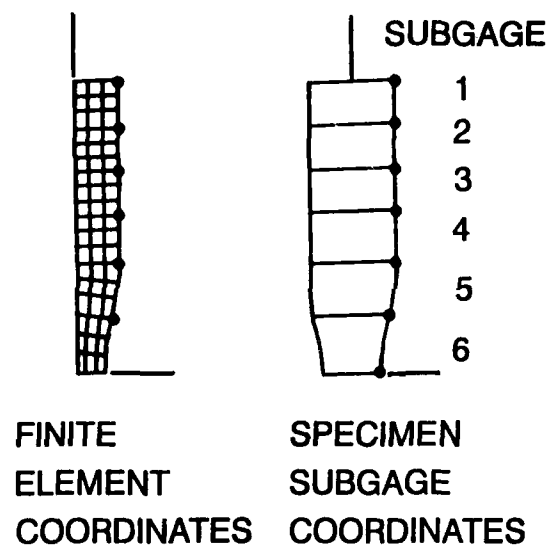


Figure 6—Computational software schematic diagram.

Comparison Software

The third step, performed iteratively in conjunction with each computational simulation of the specimens, was comparison of laboratory and computational simulation data. Software was developed to facilitate the comparison (Figure 7). Four specific goals were achieved. The first goal was to convert the digital and video laboratory data files and the computational data files to spatially and temporally equivalent representations for direct comparison. The second was the tabular representation of computational and experimental subgage surface deformation data for comparison. The third was the tabulation of the predicted constitutive response of the material within each subgage. The final goal was to modify the constitutive response for the next iteration. The entire process was repeated until satisfactory agreement was reached. Satisfactory agreement was taken to be less than five percent difference between engineering stress values over the entire engineering strain range for both specimen geometries considered in this investigation.

Implementation of the comparison software reflects user selection of experiment and simulation parameters. General parameters include specimen gage length, specimen diameter, and the number of subgages to be created from computational and experimental data. Laboratory experiment parameters include the number of laboratory times sampled. Computational simulation parameters include the number of rows and columns in the finite element mesh, element type, element numbers and quadrature points per element and the number of computational data files available from the current iteration.

For the L_0/D_0 ratios of 1.0 and 2.0 used in this investigation, symmetric specimen necking is computationally predicted. The experimental data on specimen deformation symmetry, given in Table AII, confirmed that no significant departure from symmetry was present. Small deviations from symmetry in the laboratory were anticipated. Symmetrization of the laboratory specimen profile was required so that a direct comparison of laboratory and computational data could be made. A symmetrization procedure was implemented, as shown in Figure 8, by (i) identifying global asymmetry with respect to the minimum diameter at the specimen neck, (ii) local symmetrization of radial deformation above and below the neck and (iii) global symmetrization by redistribution of the asymmetric portion of the specimen profile. A constant gage length volume condition was imposed from the end of the specimen toward the center of the symmetrized neck to facilitate symmetrization. This left the volume residual at the neck, where any hydrostatic deformation of significance would be unaffected by this symmetrization procedure. In practice, the volume residual was less than one percent of the total.

Interpolation of the computational load, surface profile and quadrature point constitutive data from the finite element computational prediction was performed within the temporal framework provided by the laboratory datafiles. The laboratory data is preferable for use as a time basis since laboratory time is physically motivated for the material. Furthermore, laboratory data was taken at equal time intervals. The pseudo-time values generated by the finite element automatic time stepping algorithm facilitate efficient computation but are, in general, irregularly spaced and do not correspond to the physical time measured in the laboratory. Interpolation of the computational data was done twice. The first interpolation is performed to obtain an engineering strain measure from the computational prediction to equate with the laboratory engineering strain. In this manner, computational pseudo-time was equated to physical time measured in the laboratory through the engineering strain measure. The second interpolation is performed on the computationally predicted load, surface displacement and constitutive quantities to generate values at the desired physical times (or engineering strains).

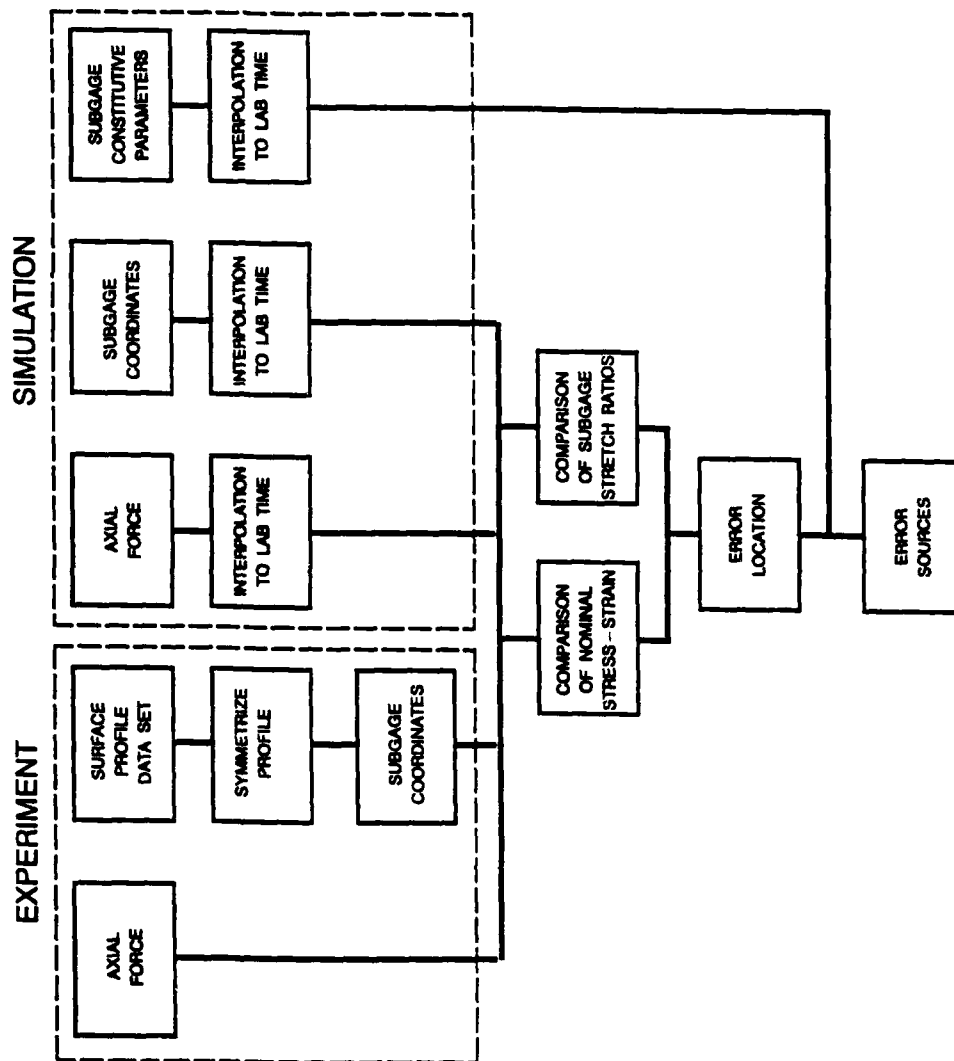


Figure 7—Comparison software flow chart.

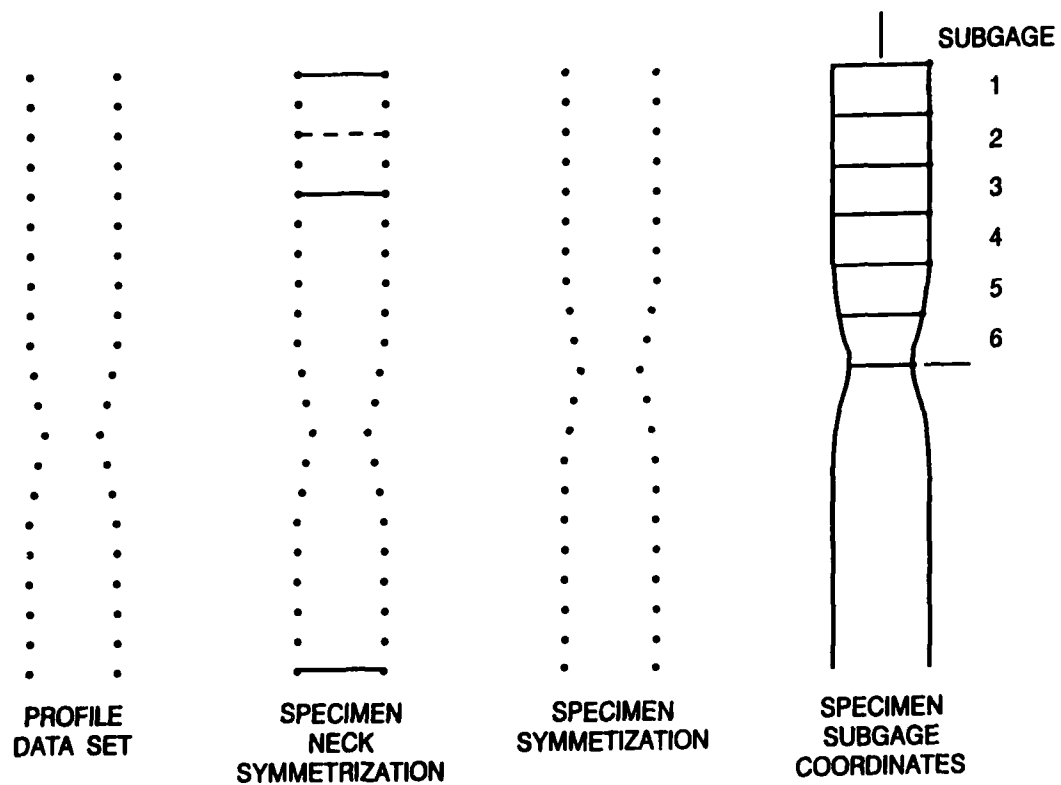


Figure 8—Comparison software profile symmetrization schematic diagram.

Six subgages were used over the half specimen lengths in this investigation. Subgage axial stretch ratio values from experimental and computational displacement data, as defined by

$${}^t\lambda_i = \frac{{}^t z_{i+1} - {}^t z_i}{{}^0 z_{i+1} - {}^0 z_i} \quad (11)$$

and

$${}^c\lambda_i = \frac{{}^t z_{i+1} - {}^t z_i}{{}^c z_{i+1} - {}^c z_i} \quad (12)$$

where ${}^t\lambda_i$ and ${}^c\lambda_i$ are the experimental and computational stretch ratios, respectively, defined from the axial displacements ${}^t z_i$ and ${}^c z_i$ at time t for the i -th subgage. The denominator of both expressions are, of course, equal at zero time since the laboratory and computational experiments are identical. The ratio of these two quantities,

$${}^t R_i = \frac{{}^t\lambda_i}{{}^c\lambda_i} \quad (13)$$

was used to identify subgage surface displacement errors at the onset of global specimen response errors. As anticipated, the subgage responses nearest to the neck contraction were influenced by the largest material deformations within the specimen gage volume.

Effective plastic strain values at each quadrature point for a given load were sorted into intervals by strain and subgage location. This matrix was tabulated to create a set histogram of the specimen constitutive response. The tabulated effective plastic strain is identical to the uniaxial plastic strain of the constitutive parameters by virtue of the constants used in the constitutive formulation to relate uniaxial and multiaxial deformation states. The histogram of the computational simulation, at the load corresponding to the departure from laboratory experiment, identified the range of constitutive parameter values which did not accurately represent the material response. This range was addressed in the corresponding constitutive parameter iterations discussed below.

It should be noted that since the quadrature point histograms were defined as a set measure, they did not represent the volume weighted contribution to the subgage volume in question. That is to say, the quadrature point values near the axisymmetric specimen surface contribute more to the effective strain histogram than do quadrature point values near the longitudinal axis of the specimen according to their volume integration over respective finite elements. Therefore, the set histograms employed here identify the range of constitutive parameter values encountered in a given subgage volume. The effect of this simplification on parameter iteration is marginal in view of the range of multiaxial, path dependent deformation states present in the subgage of most severe deformation and the fact that the histogram use lies outside of the computational simulation.

Constitutive Parameter Determination Iterative Strategy

The analysis sequence described in the following discussion was developed with the intent of obtaining an accurate solution for the HSLA-80 steel, keeping computational costs low and avoiding the complications caused by broken deformation symmetry at higher L_0/D_0 ratios (as was observed for HY-100 specimens by Matic et al (1988)). As anticipated, Specimen No. 1 featured an extensive range of diffuse nonlinearity due to neck development over its entire gage length. This allowed easy

access to a broad range of material responses within the specimen from a computationally small model. Specimen No. 2 featured a fully developed neck with large deformations and, in regions outside the neck but still within the bounds of the specimen gage length, material which loaded and unloaded through moderate deformations. In this case, the combined influence of the extensive, monotonically increasing, spatially inhomogeneous deformation within the neck volume and the moderate deformation in the specimen volume outside the neck affect the global specimen response dependent upon the relative balance of constitutive parameters simultaneously governing deformation in both regions. In this manner, the two tensile specimen geometries complement one another in the constitutive solution process.

The analysis sequence provided insight for iteration strategy. Each comparison between computational prediction and experimental data was used to guide the identification of solution curve intervals requiring modification for the next iteration in terms of equivalent uniaxial stress and strain ranges beyond the largest Cauchy stress and log strain values accepted as the material constitutive solution curve. The sequence is described below.

Step 1—The engineering stress and engineering strain responses from the computational and experimental data, $(\bar{\sigma}, \bar{\epsilon})_c$ and $(\bar{\sigma}, \bar{\epsilon})_e$ respectively, were plotted on one pair of axes. The form of the data was evaluated to determine whether the load monotonically increased or reached a peak value followed by a decrease. If a peak occurred, the stress and strain at which a peak occurred and the post peak behavior are directly related to the ease at which material flow takes place within the actively yielding neck volume. Most importantly, the strain at which the computational prediction departed from the experimental data identifies the onset of relative stiffness or softness in the candidate material parameters beyond those already determined to satisfy the comparison to a specified level of error. As discussed above, the computational strain was used to identify the pseudo time in the case of rate independent material response (for which no natural time scale exists). Therefore, the load is the true independent measure of the constitutive parameter accuracy in predicting both local and global specimen response.

Step 2—Computational and experimental subgage stretch ratios ${}^t\lambda_i$ and ${}^e\lambda_i$, defined by each adjacent set of subgage boundaries, were calculated and the ratio of computational to experimental elongations tR_i tabulated. This information was used to identify the location and magnitude of subgage elongation errors along the specimen.

Step 3—Constitutive response histograms were tabulated from the computational data generated by test specimen simulation. Histograms for each subgage volume were tabulated to identify the range of constitutive parameters which governed predicted subgage deformation. The histograms allowed precise determination of constitutive error sources by facilitating comparison between elongation errors and the relative intensity of the deformation state occurring within a subgage volume.

Step 4—On the basis of the comparisons between computationally predicted and experimentally observed surface data and the predicted local constitutive response internal to the specimen boundaries, an improved iteration for constitutive parameters was developed.

For ductile steel alloys, such as the HSLA-80 alloy under consideration, changes in the stress parameters of approximately 0.05 times the current iteration value of the stress were sufficient to produce comparable changes in the specimen axial force prediction. Changes of approximately 0.10 times the current strain values, carried through from the first strain value changed to the largest strain value in the constitutive parameter set, generated comparable changes in the global ductility of the computational prediction. These values indicate, in a quantitative manner, the sensitivity of the iterative strategy employed here.

Results for HSLA-80 Alloy

Implementation of the iteration strategy for the HSLA-80 alloy is as follows. The small strain engineering stress-engineering strain response of all four laboratory HSLA specimen geometries (Figure 3) was observed to be relatively insensitive to the specimen geometry in the range $0.00 < \bar{\epsilon} < 0.10$. Within this relatively small strain range, a power law of the form

$$\sigma = \sigma_y + A \epsilon^n \quad (14)$$

was used to fit the data and provide extrapolated values at higher strains for Iteration No. 1 of the constitutive parameters. The experimental HSLA-80 data suggests values for these parameters so that the expression is

$$\sigma = 82000 + 68.57 \epsilon^{0.66} \quad (15)$$

A multilinear approximation of this power law was determined, consistent with the nonlinear material response format for the finite element model, in the form of uniaxial Cauchy stress-log plastic strain pairs, i.e. (σ, ϵ^p) . These parameters, used in Iteration No. 1, generated the uniaxial $\sigma - \epsilon$ curve used for constitutive calculations (Figure 9). The upper limit of the strain range was selected to exceed the logarithmic strain at fracture, approximated by the axial logarithmic strain using the cross section area ratio at fracture., i.e.

$$\epsilon_f = \ln \frac{A_0}{A_f} \quad (16)$$

where A_0 is the original specimen area and A_f is the neck area at specimen fracture. For HSLA-80, the area ratio at specimen fracture was approximately five. Therefore, the constitutive parameter range considered exceeded a uniaxial log strain of 1.60. The actual fracture point on the constitutive solution curve is dependent upon on the local stress, strain and strain energy density histories and the microstructural features which govern continuum inelasticity and energy dissipation. This point is determined from the experimental data and computationally predicted deformation state at the center of the neck for each specimen.

The constitutive parameter iteration sequence can best be described in terms of the computational simulation number (1,2,3, ...), the specimen geometry (No. 1 or 2) and the constitutive parameter set iteration number (1,2,3,...). Five computational simulations of Specimen No. 1, featuring the lowest L_0/D_0 ratio and large deformations throughout the gage length, were used to generate successive constitutive parameter iterations No. 1 through 5 (Figures 9-13). The iteration sequence initially involved changes to both stress and strain values, followed by strain values alone, followed by stress values alone. Agreement between computational prediction and experiment after the fifth constitutive iteration suggested that the general nonlinear form of the HSLA-80 material response had been obtained.

Computational simulations proceeded by changing to the geometry of Specimen No. 2. The first computational simulation on this specimen, using the last constitutive parameter set obtained from Specimen No. 1, indicated some errors remained in the constitutive parameters. Successive corrections to the constitutive parameter stress values were developed. Good agreement was reached after four computational simulations and constitutive parameter modifications of Specimen No. 2 (Figures 14-17). Confirmation of the constitutive solution curve was made by a final computational simulation,

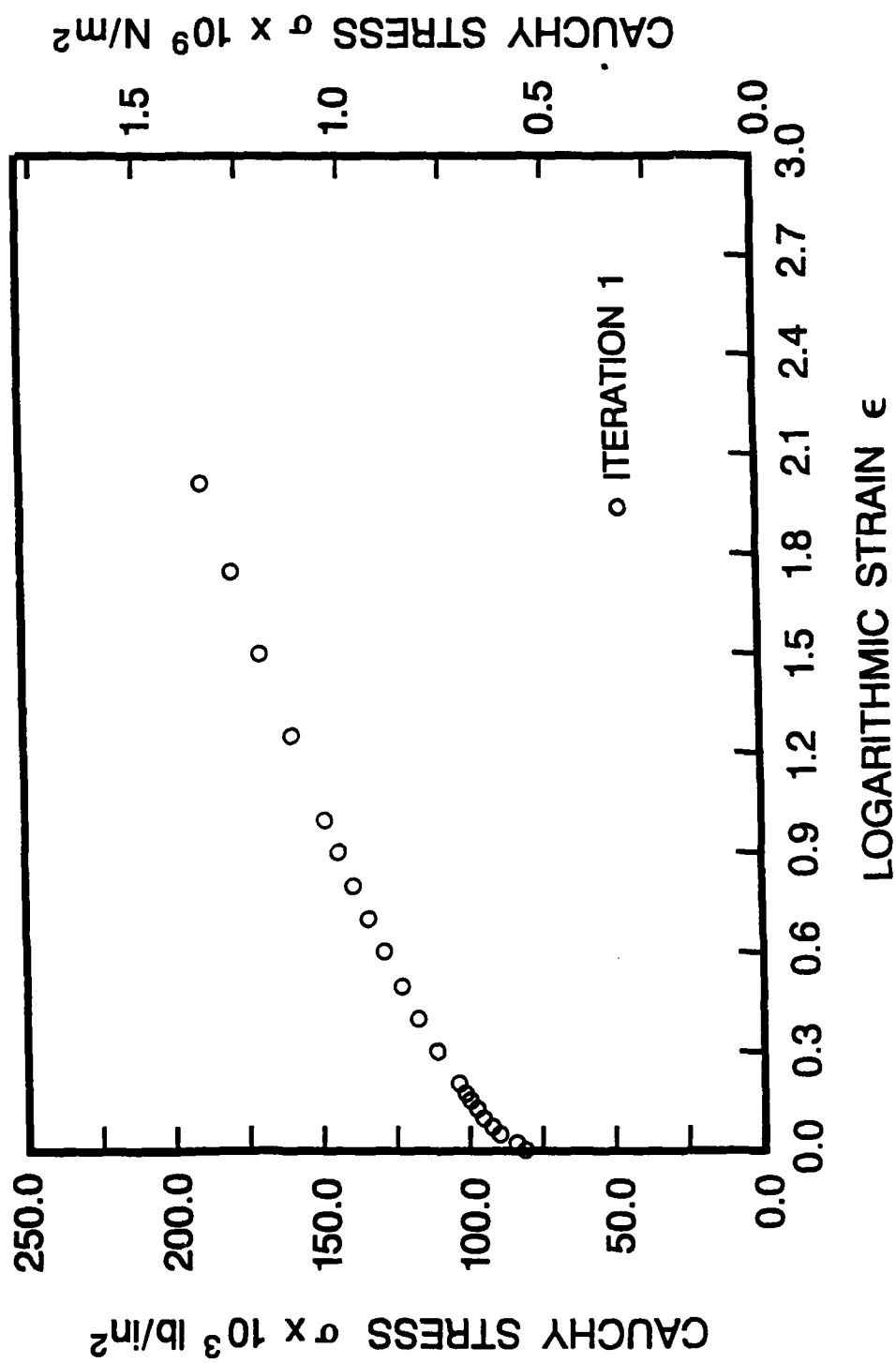


Figure 9—Computational Simulation 1 using Specimen 1, (a) Constitutive Iteration 1 obtained from power law fit and extrapolation of small strain data, (b) $\bar{\sigma}$ - $\bar{\epsilon}$ comparison.

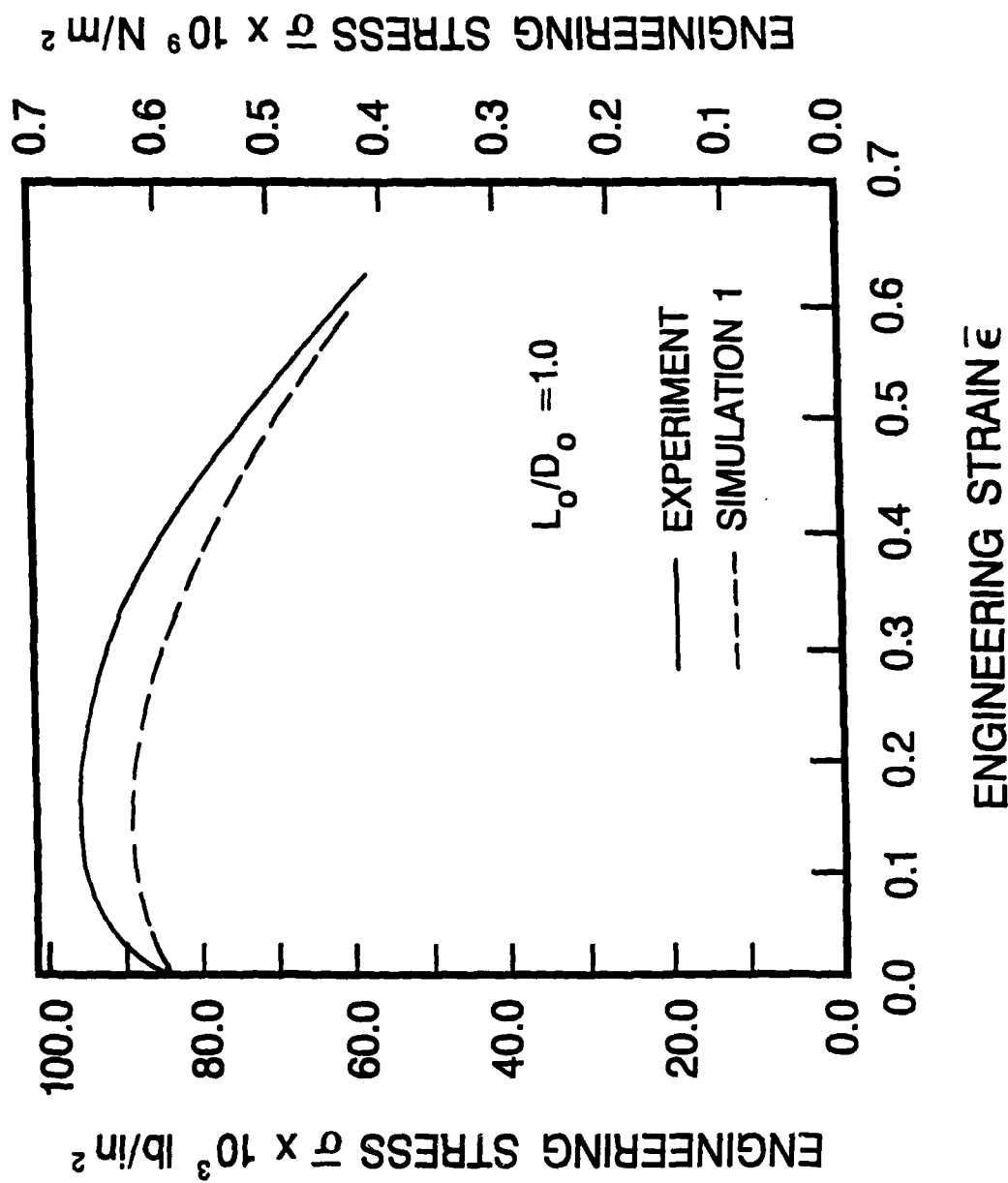


Figure 9 (Continued) — Computational Simulation 1 using Specimen 1, (a) Constitutive Iteration 1 obtained from power law fit and extrapolation of small strain data, (b) $\bar{\sigma} - \bar{\epsilon}$ comparison.

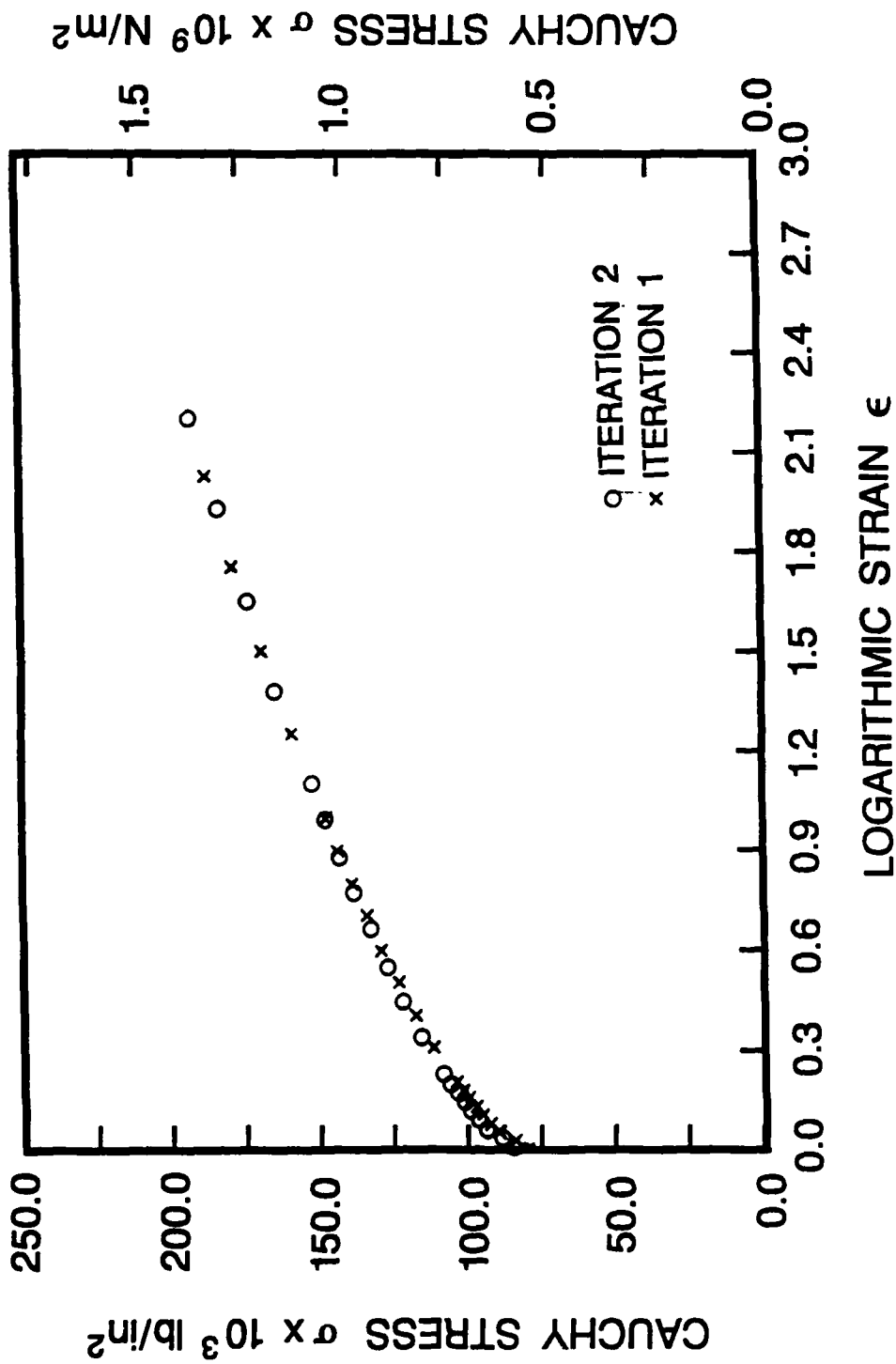


Figure 10—Computational Simulation 2 using Specimen 1, (a) Constitutive Iteration 2 (obtained by modification of Iteration 1), (b) $\bar{\sigma} - \bar{\epsilon}$ comparison.

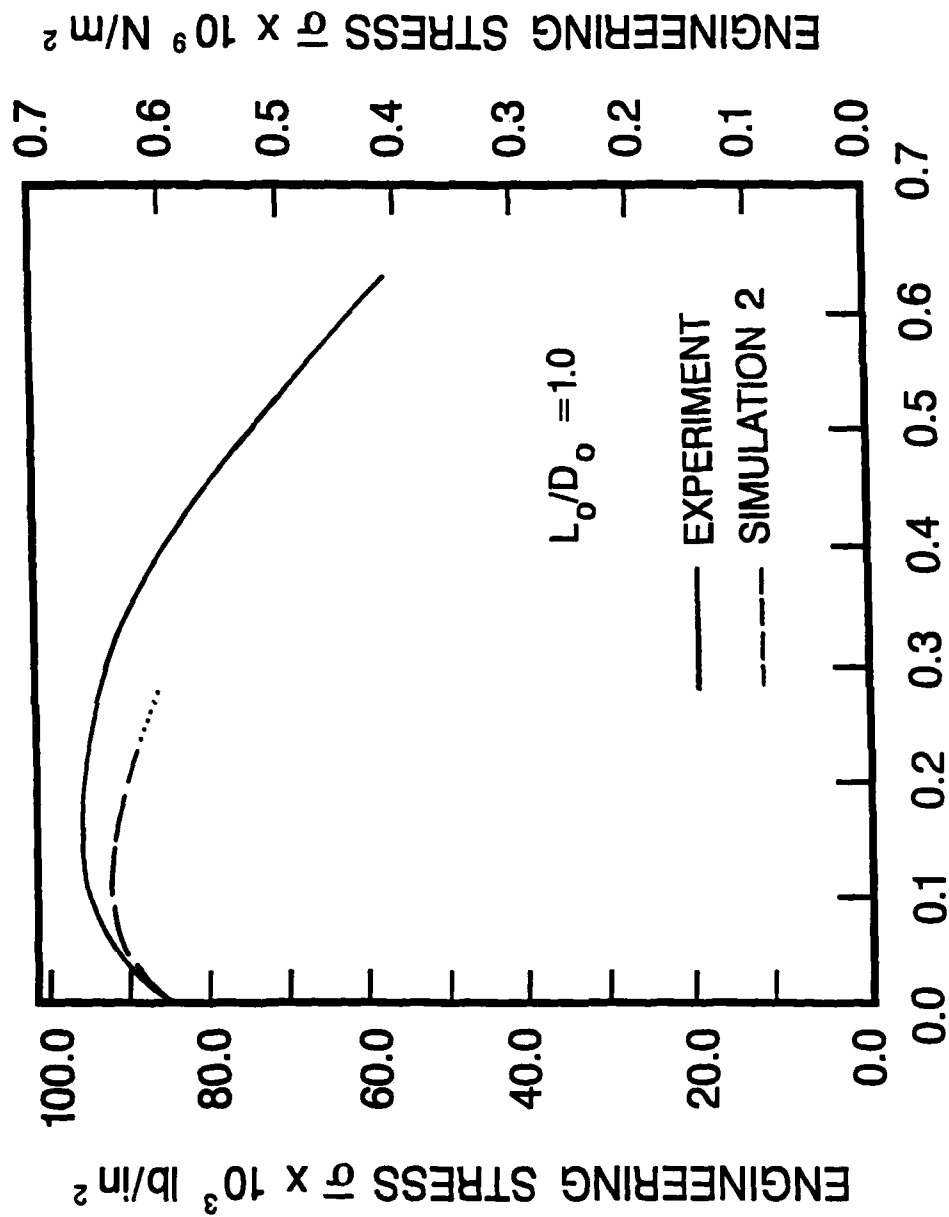


Figure 10 (Continued) — Computational Simulation 2 using Specimen 1, (a) Constitutive Iteration 2 (obtained by modification of Iteration 1), (b) $\bar{\sigma} - \bar{\epsilon}$ comparison.

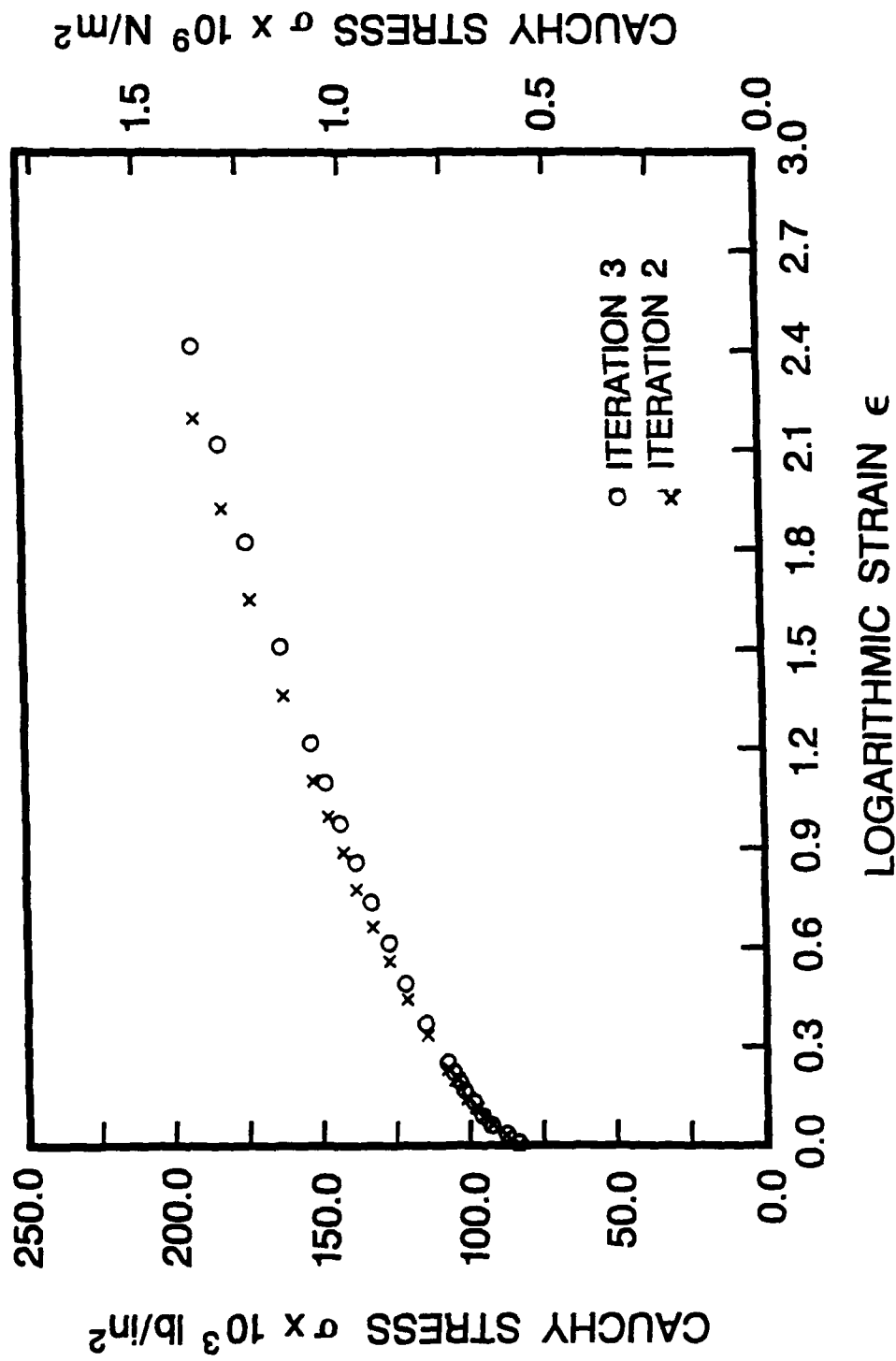


Figure 11—Computational Simulation 3 using Specimen 1, (a) Constitutive Iteration 3 (obtained by modification of Iteration 2), (b) $\bar{\sigma}$ - $\bar{\epsilon}$ comparison.

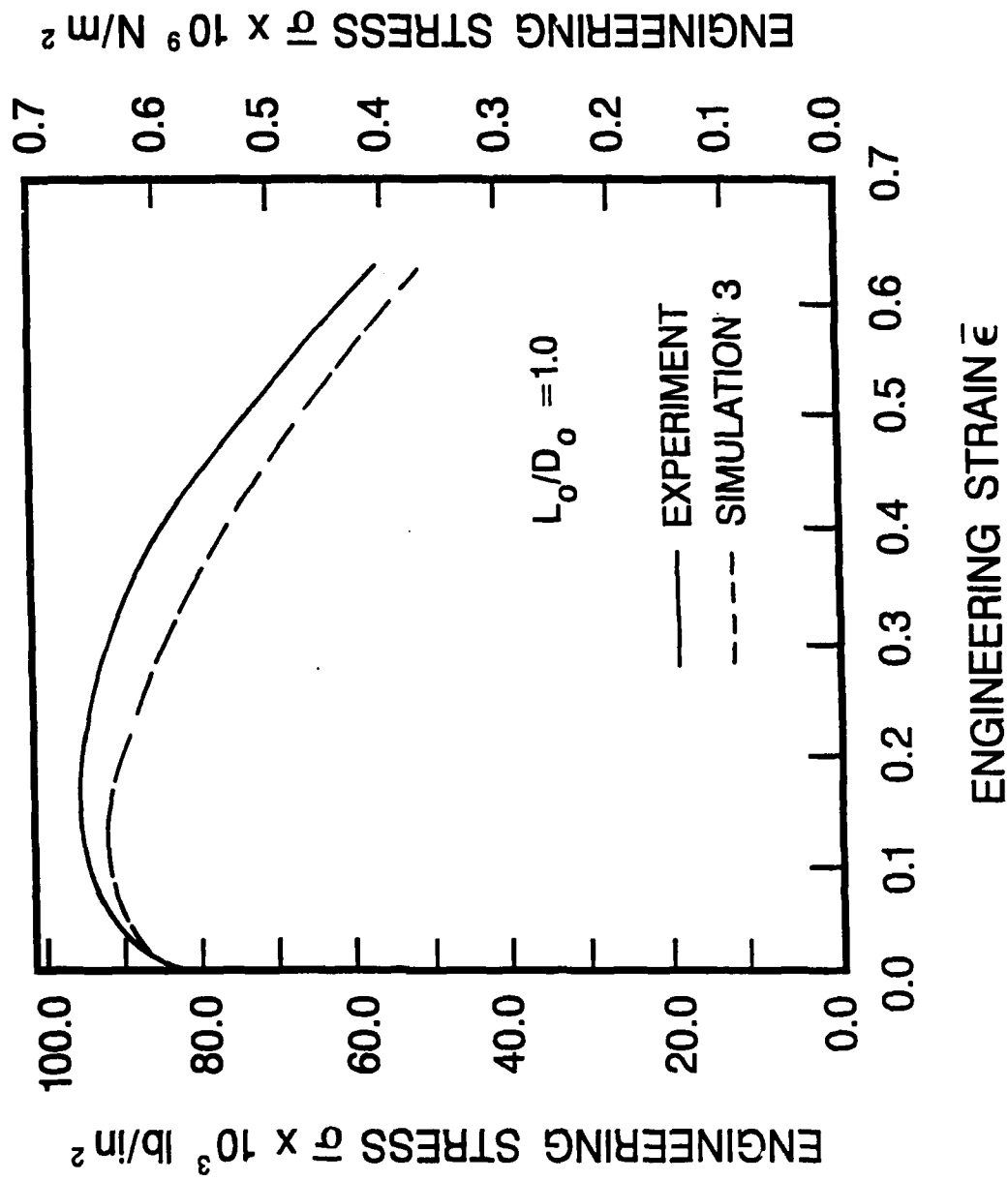


Figure 11 (Continued) — Computational Simulation 3 using Specimen 1, (a) Constitutive Iteration 3 (obtained by modification of Iteration 2), (b) $\bar{\sigma}$ — $\bar{\epsilon}$ comparison.

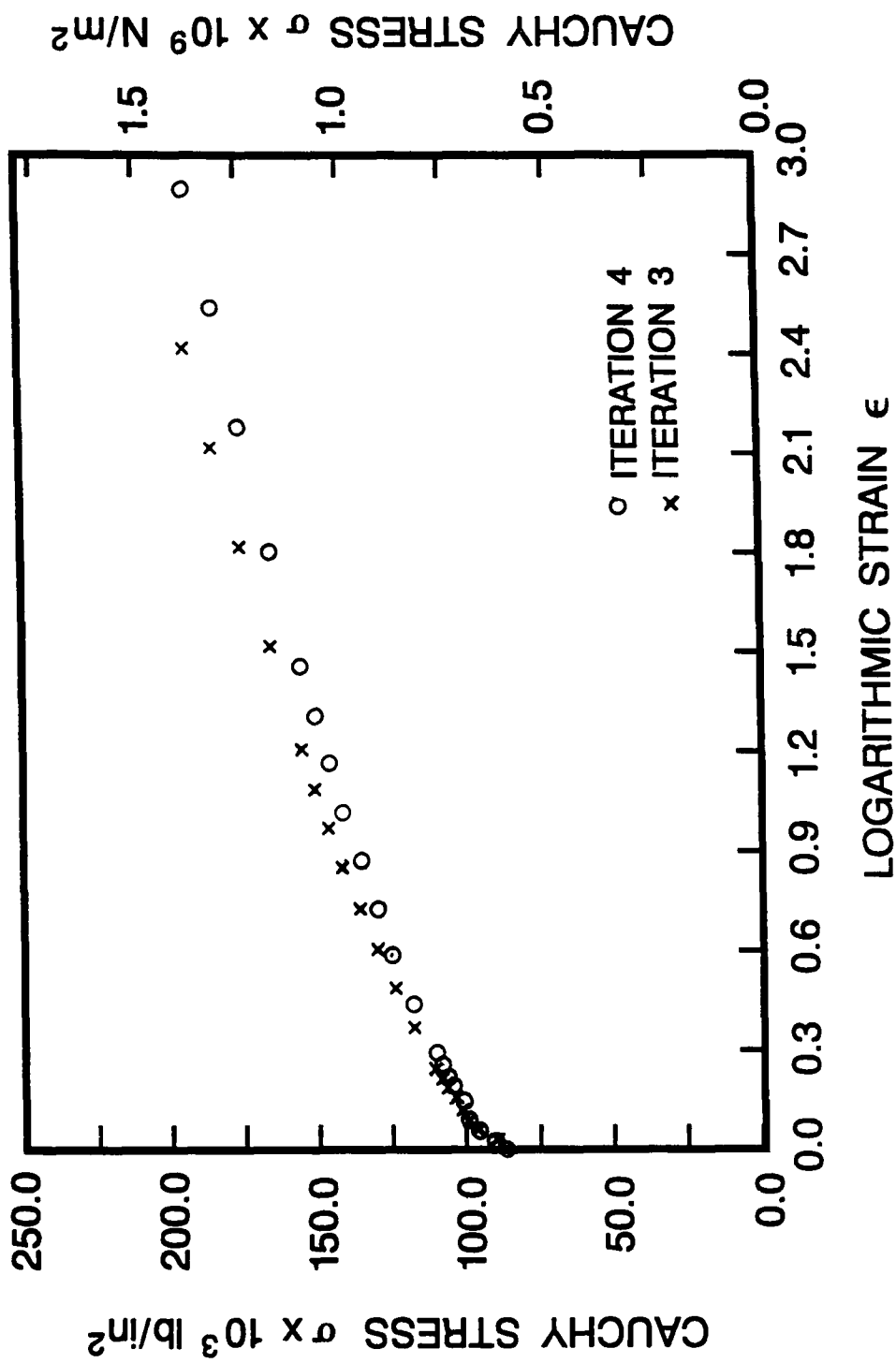


Figure 12—Computational Simulation 4 using Specimen 1, (a) Constitutive Iteration 4 (obtained by modification of Iteration 3), (b) $\bar{\sigma} - \bar{\epsilon}$ comparison.

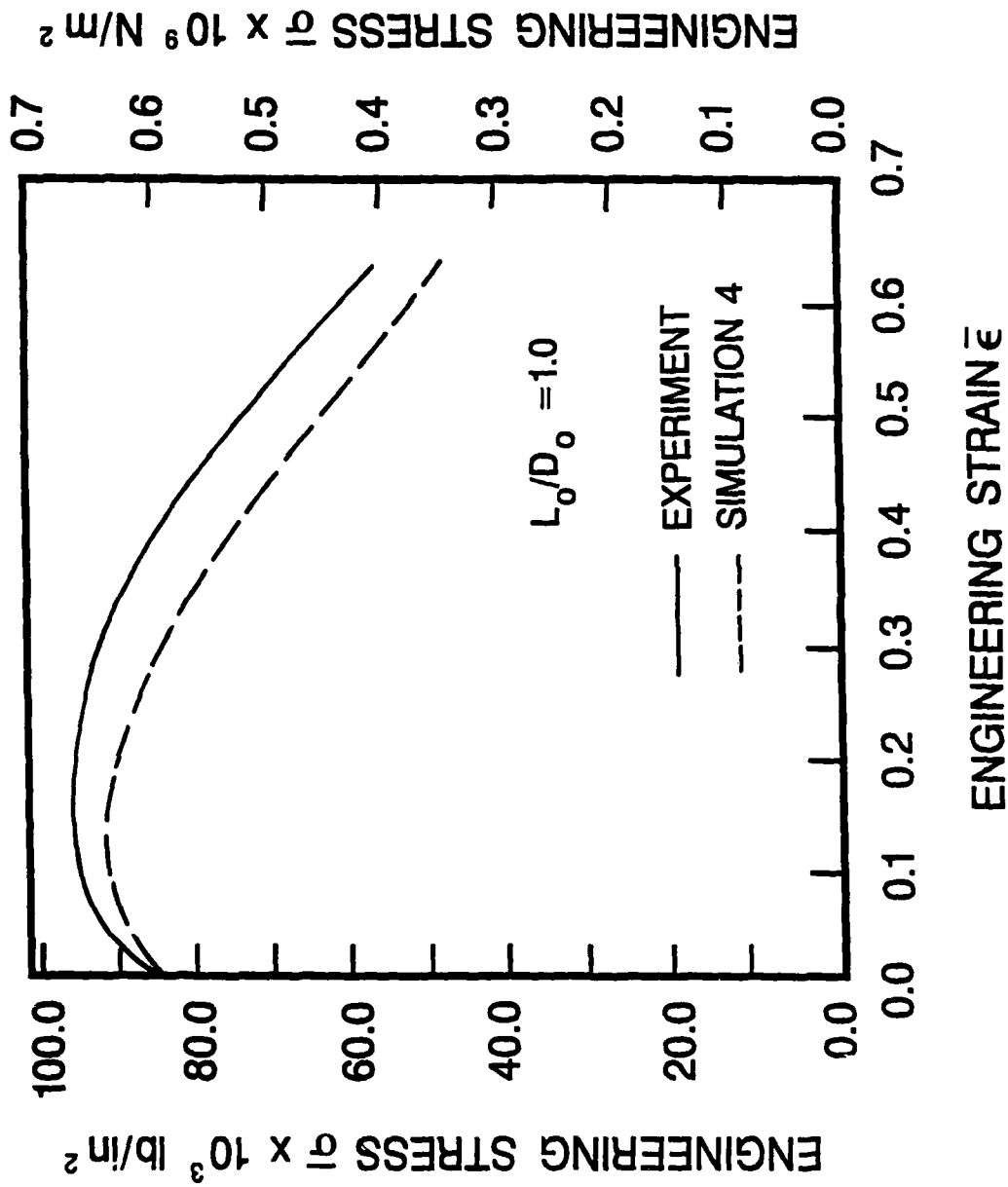


Figure 12 (Continued) — Computational Simulation 4 using Specimen 1, (a) Constitutive Iteration 4 (obtained by modification of Iteration 3), (b) $\bar{\sigma}$ — $\bar{\epsilon}$ comparison.

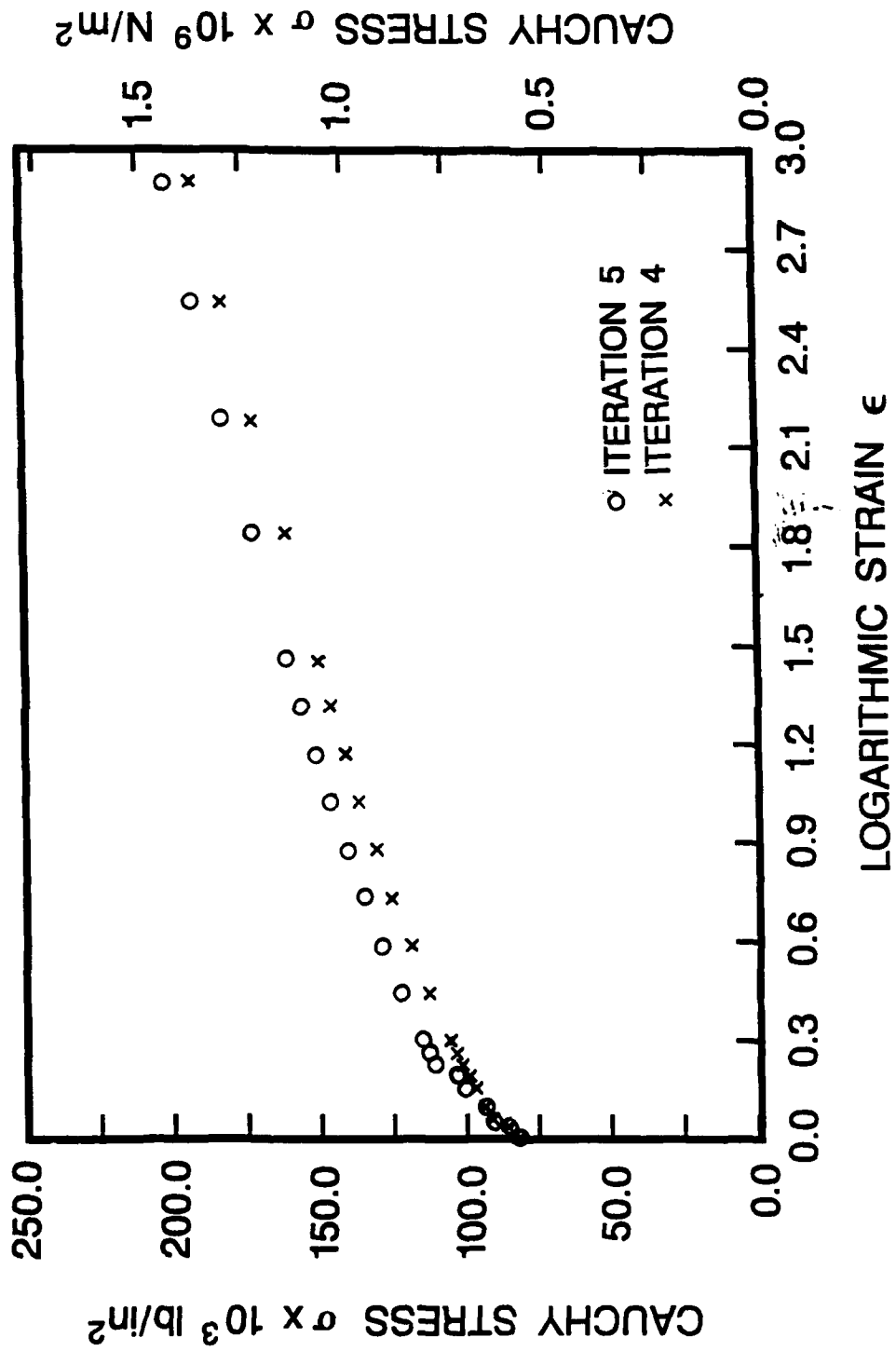


Figure 13—Computational Simulation 5 using Specimen 1, (a) Constitutive Iteration 5 (obtained by modification of Iteration 4), (b) $\bar{\sigma} - \bar{\epsilon}$ comparison.

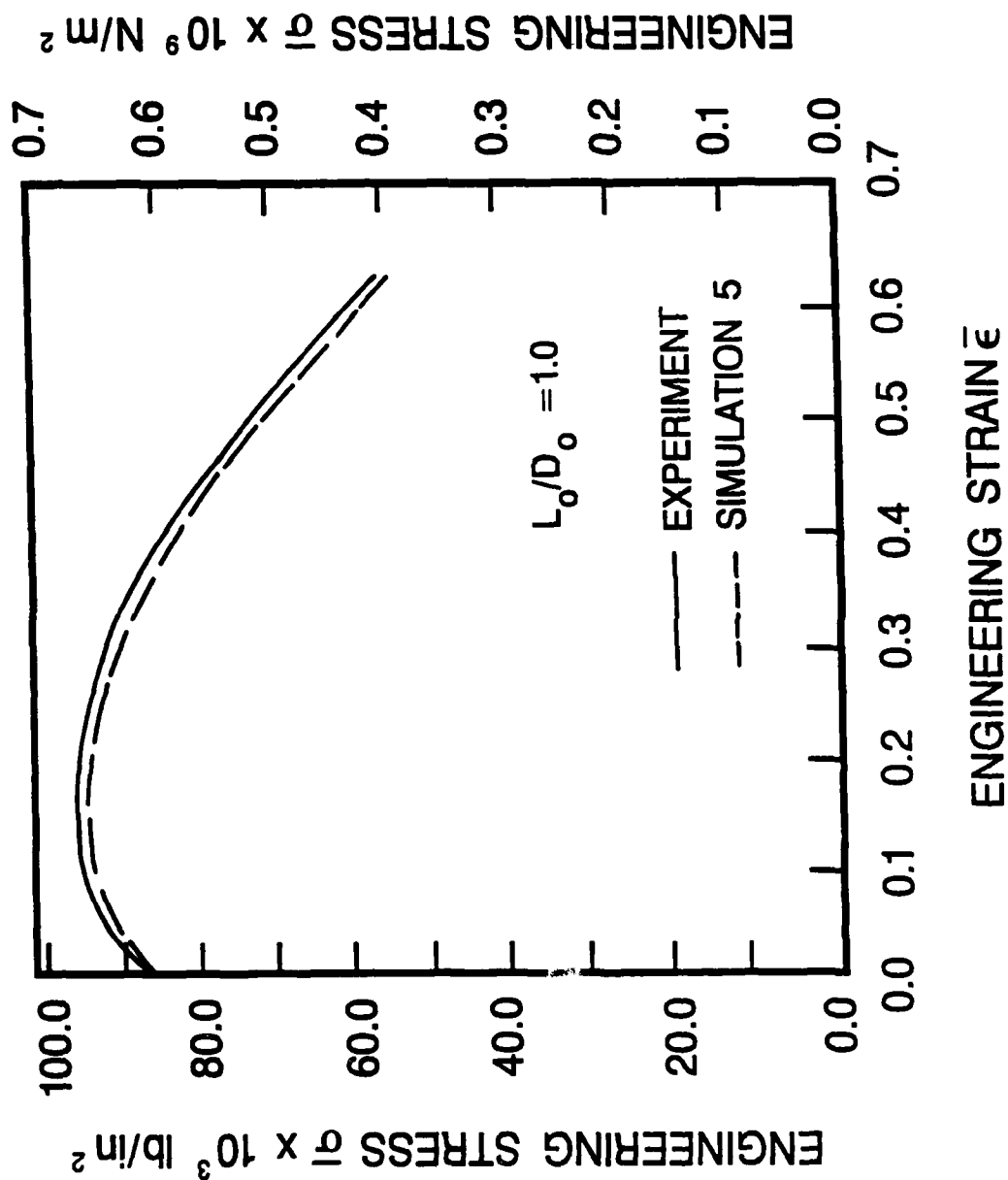


Figure 13 (Continued) — Computational Simulation 5 using Specimen 1, (a) Constitutive Iteration 5 (obtained by modification of Iteration 4), (b) $\bar{\sigma}$ — $\bar{\epsilon}$ comparison.

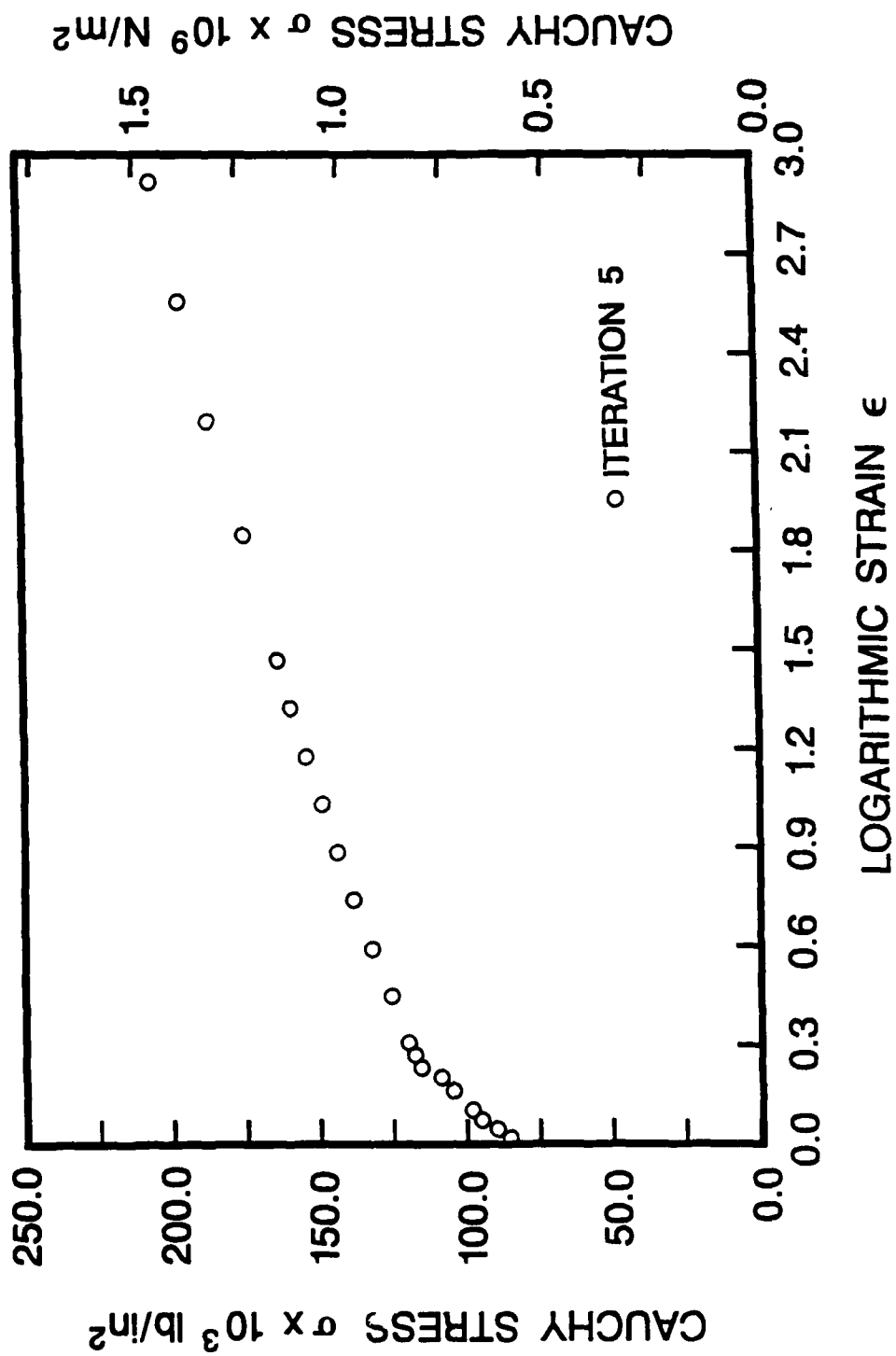


Figure 14—Computational Simulation 6 using Specimen No. 2, (a) Constitutive Iteration 5, (b) $\bar{\sigma} - \bar{\epsilon}$ comparison.

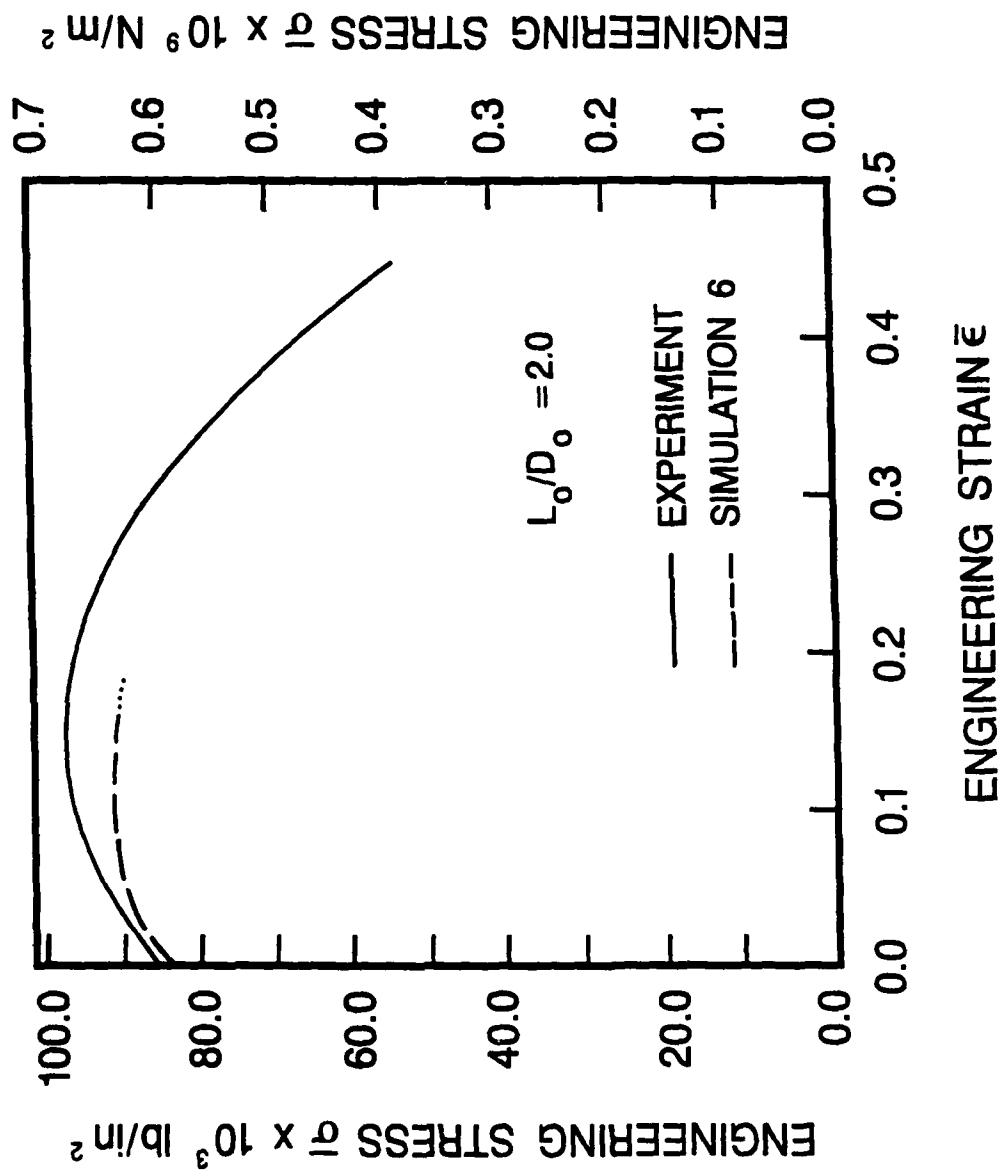


Figure 14 (Continued) — Computational Simulation 6 using Specimen No. 2, (a) Constitutive Iteration 5, (b) $\bar{\sigma} - \bar{\epsilon}$ comparison.

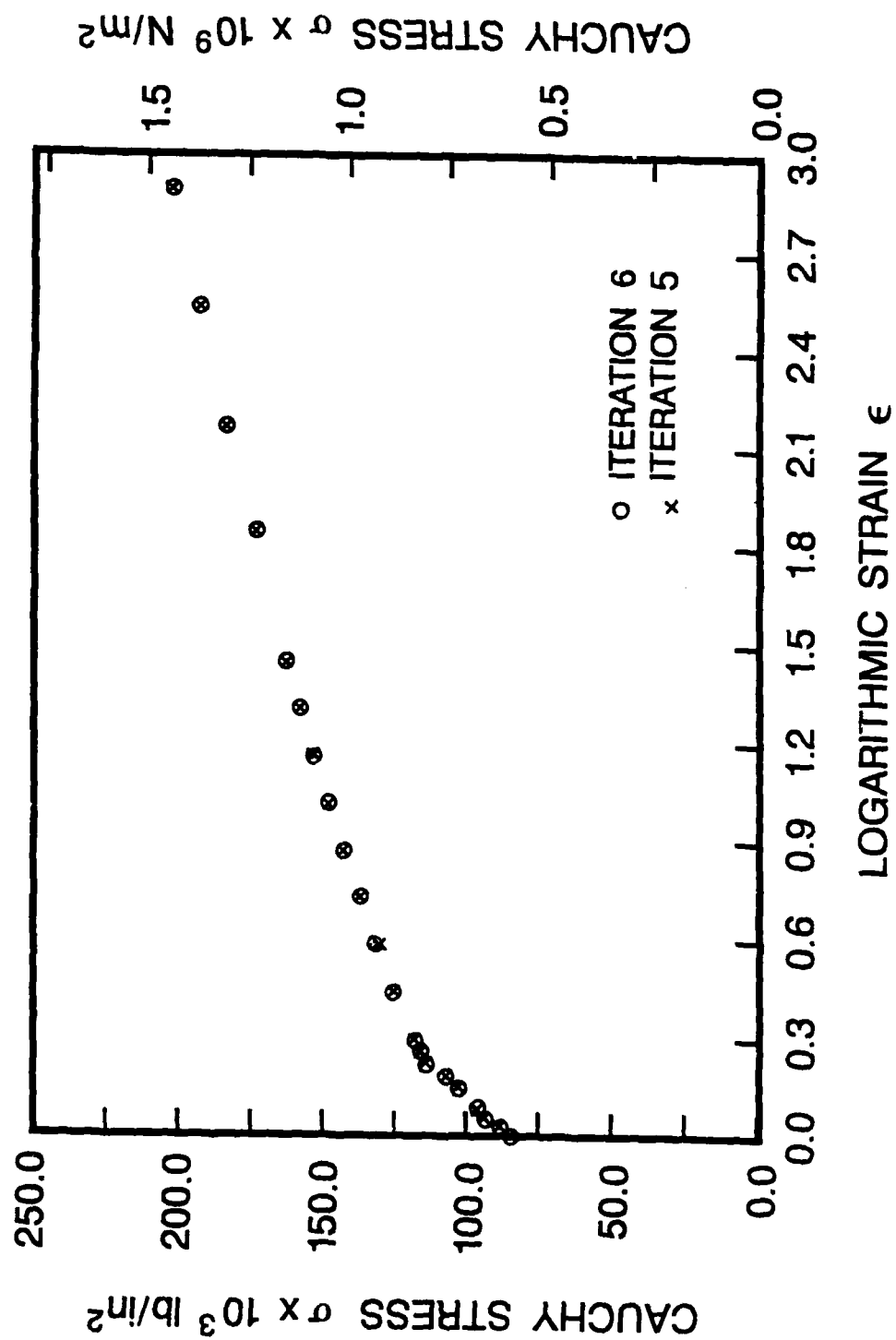


Figure 15—Computational Simulation 7 using Specimen No. 2, (a) Constitutive Iteration 6 (obtained by modification of Iteration 5), (b) $\bar{\sigma} - \bar{\epsilon}$ comparison.

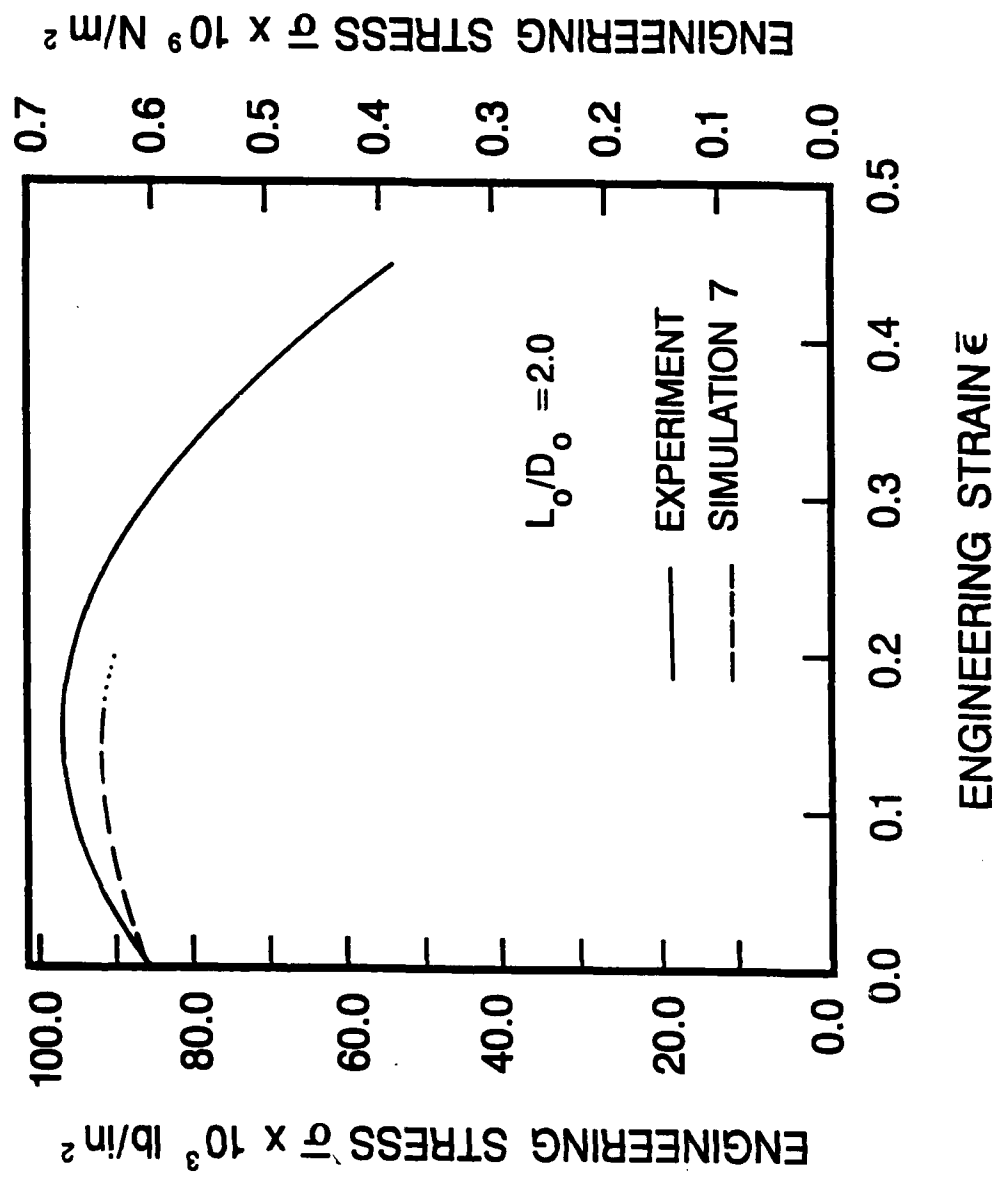


Figure 15 (Continued) — Computational Simulation 7 using Specimen No. 2, (a) Constitutive Iteration 6 (obtained by modification of Iteration 5), (b) $\bar{\sigma}$ - $\bar{\epsilon}$ comparison.

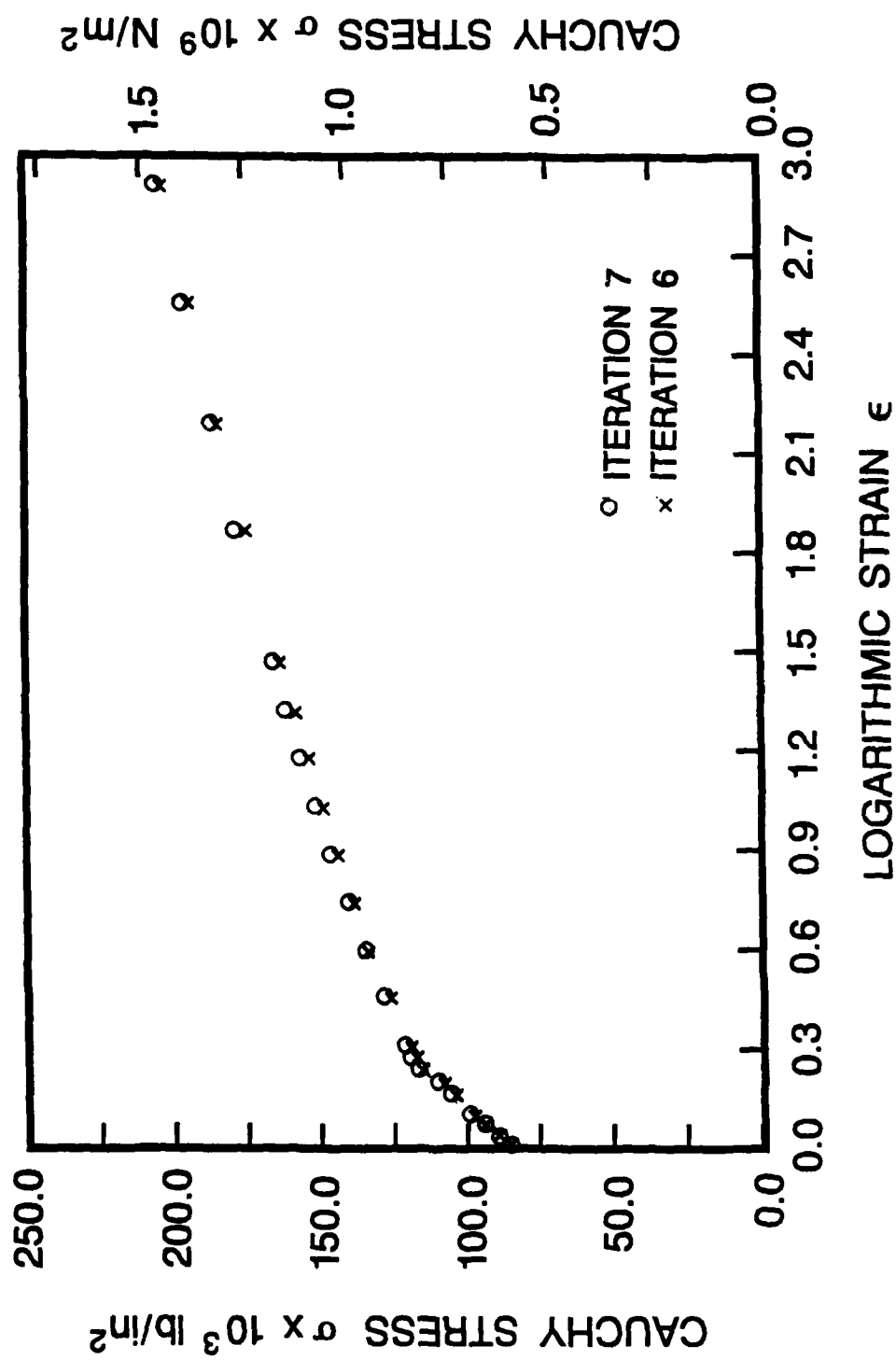


Figure 16—Computational Simulation 8 using Specimen No. 2, (a) Constitutive Iteration 7 (obtained by modification of Iteration 6), (b) $\bar{\sigma} - \bar{\epsilon}$ comparison.

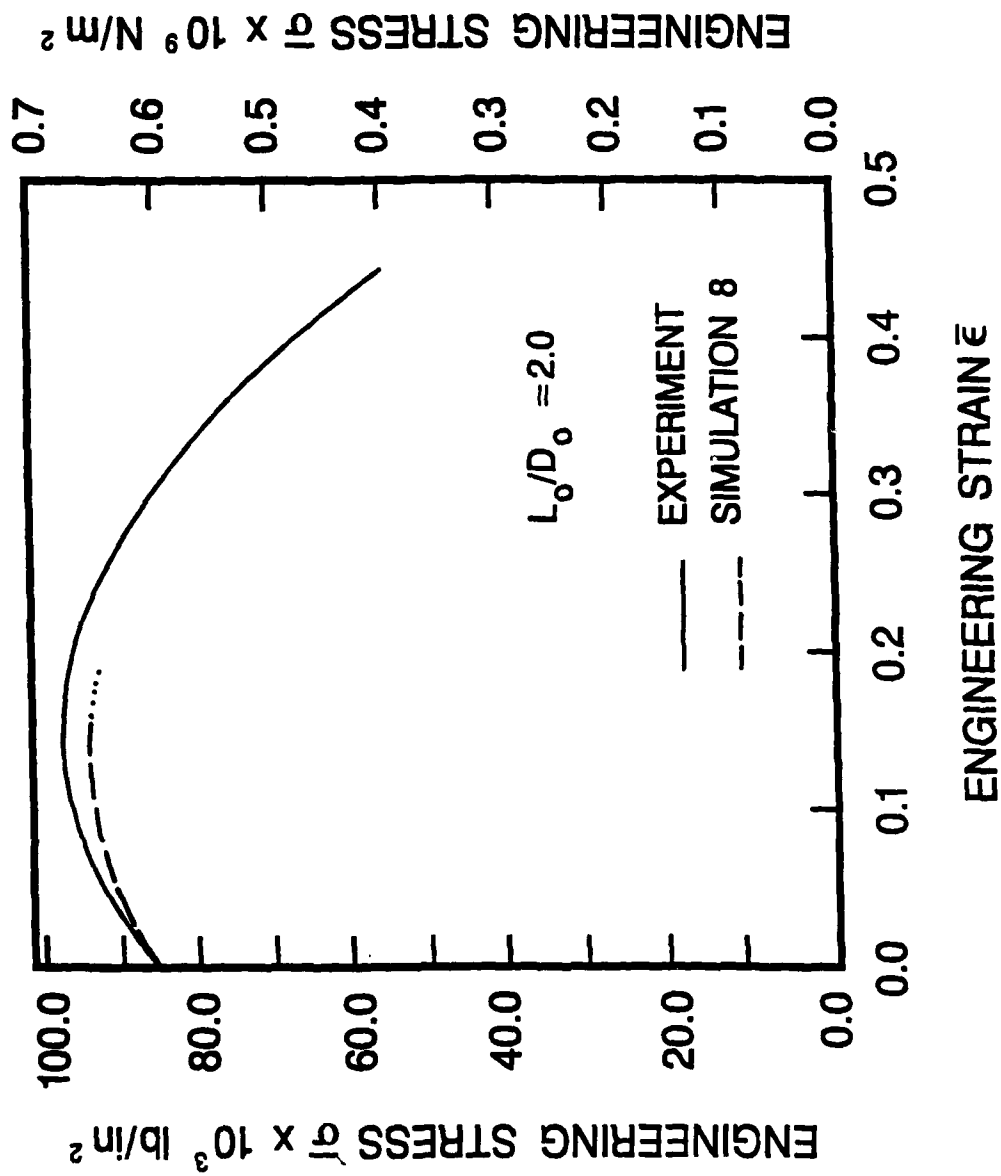


Figure 16 (Continued) — Computational Simulation 8 using Specimen No. 2, (a) Constitutive Iteration 7 (obtained by modification of Iteration 6), (b) $\bar{\sigma} - \bar{\epsilon}$ comparison.

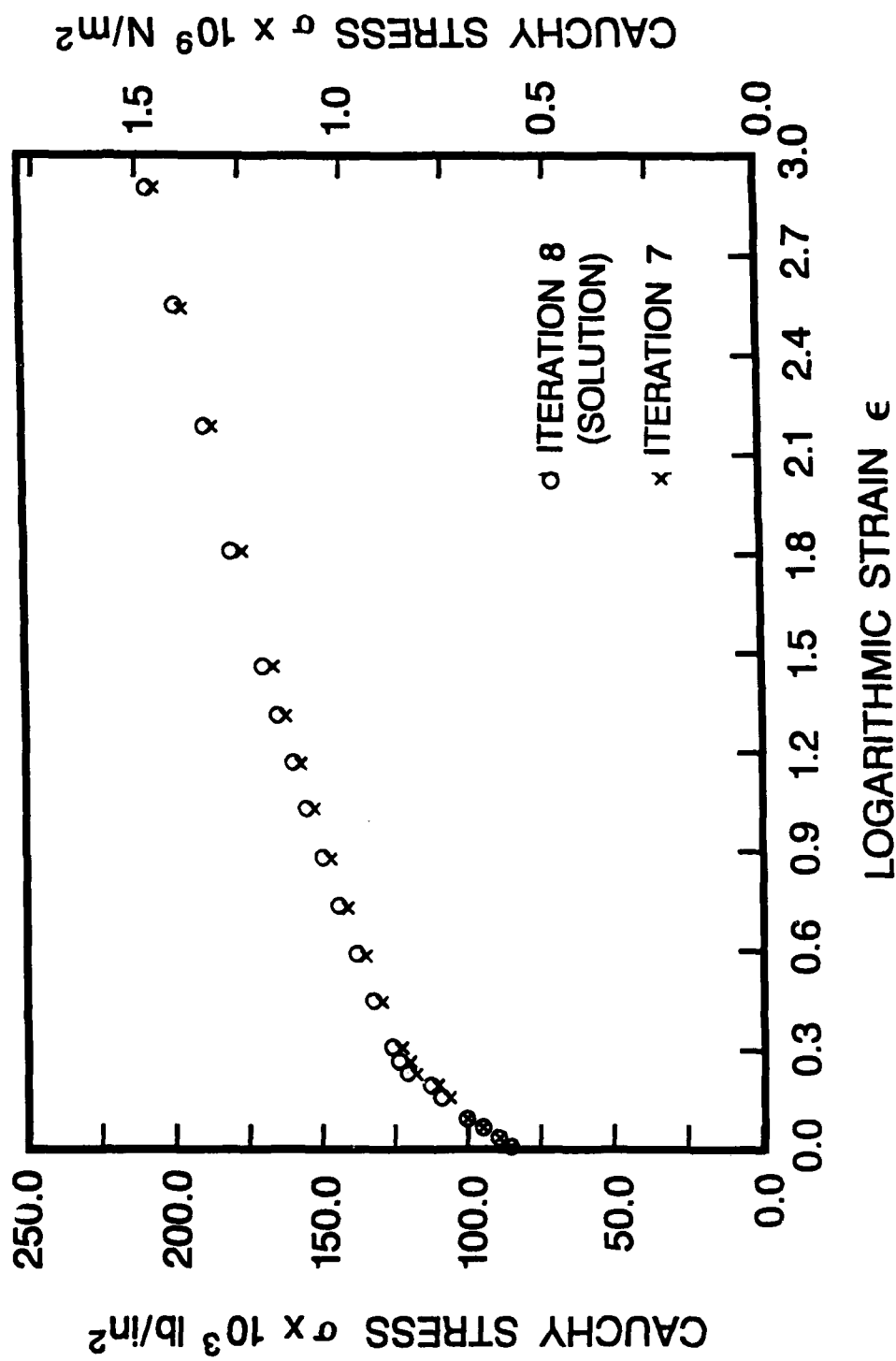


Figure 17—Computational Simulation 9 using Specimen No. 2, (a) Constitutive Iteration 8 (obtained by modification of Iteration 7), (b) $\bar{\sigma} - \bar{\epsilon}$ comparison.

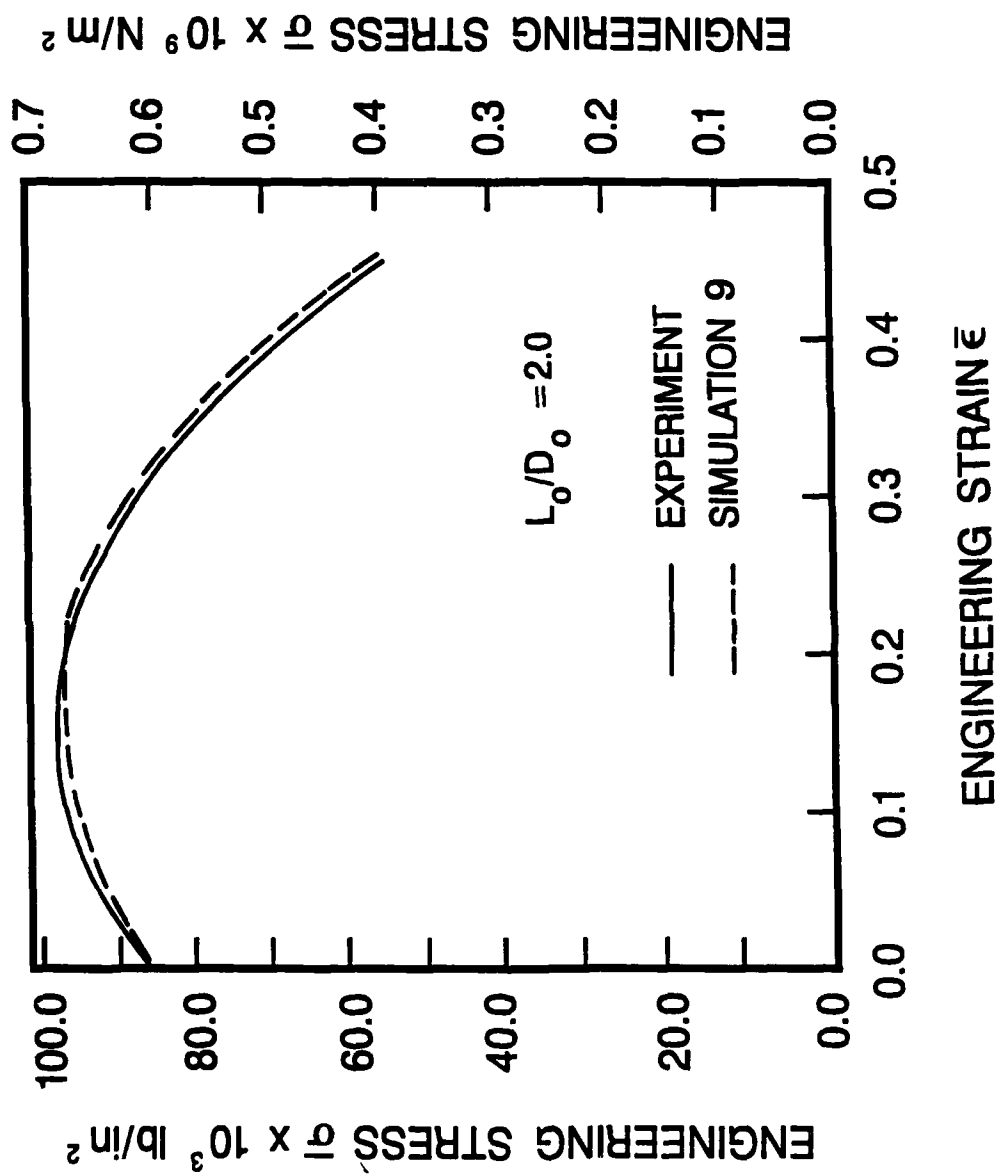


Figure 17 (Continued) — Computational Simulation 9 using Specimen No. 2, (a) Constitutive Iteration 8 (obtained by modification of Iteration 7), (b) $\bar{\sigma} - \bar{\epsilon}$ comparison.

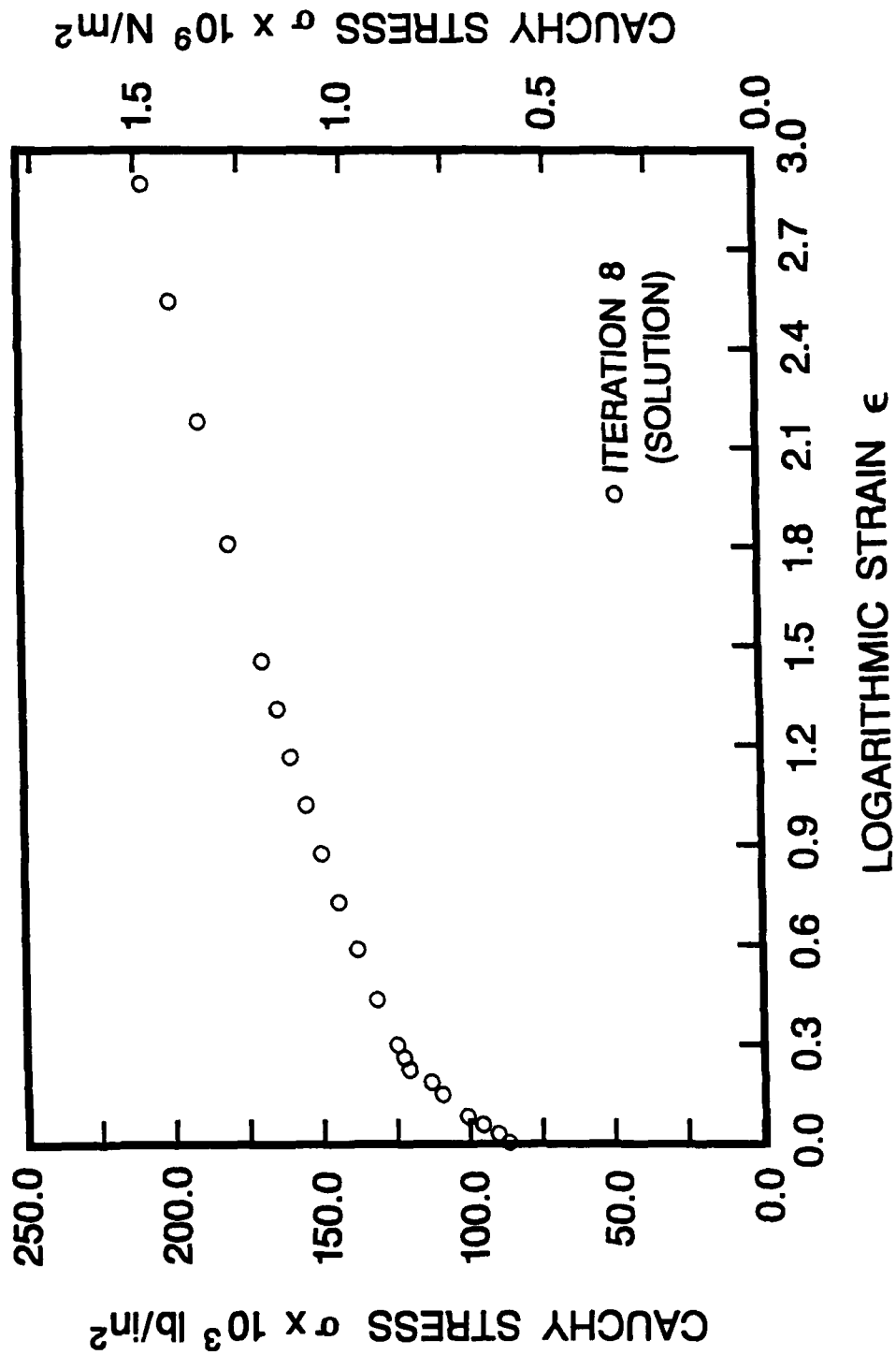
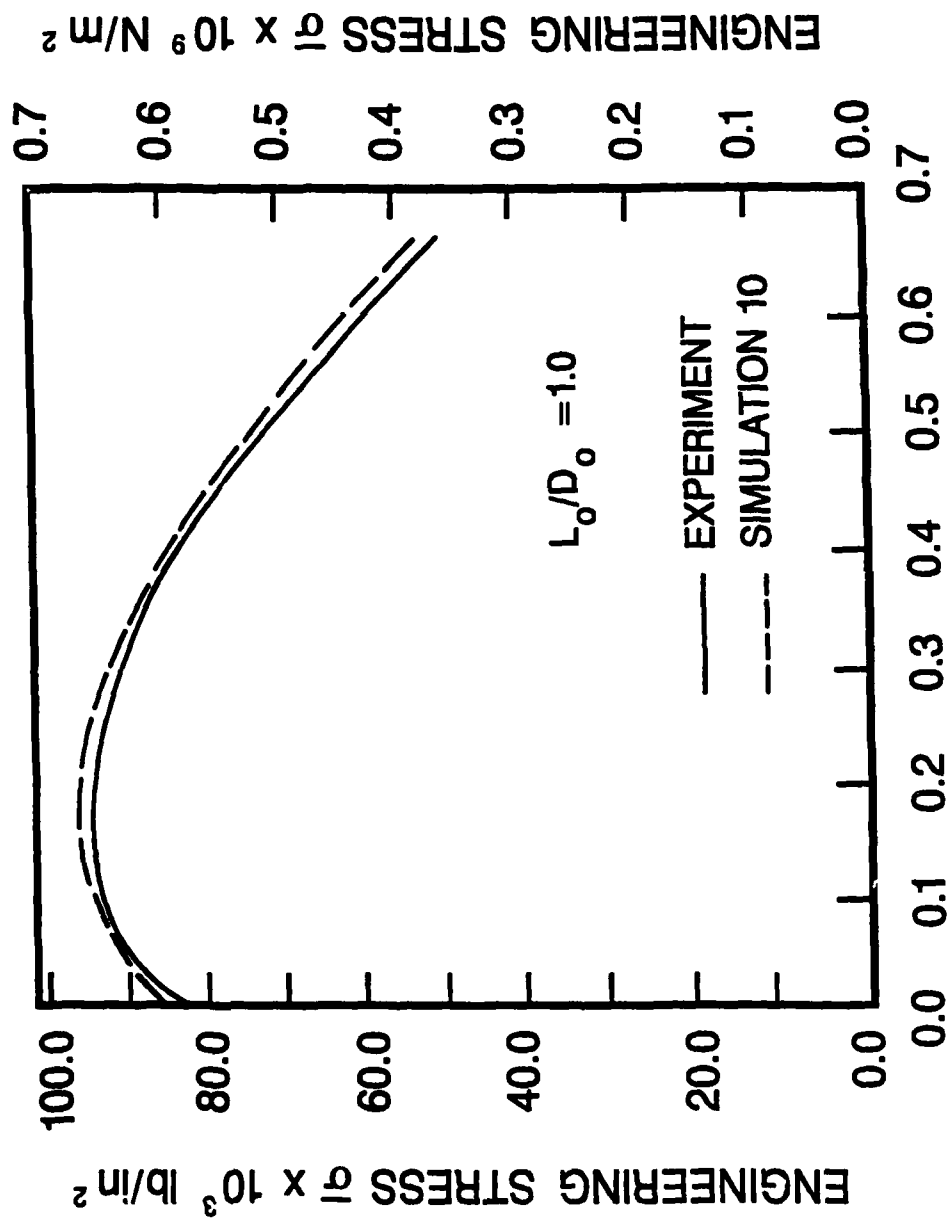


Figure 18—Computational Simulation 10 using Specimen No. 1, (a) Constitutive Parameter Set No. 8, (b) $\bar{\sigma}$ - $\bar{\epsilon}$ comparison.



ENGINEERING STRAIN $\bar{\epsilon}$

Figure 18 (Continued) — Computational Simulation 10 using Specimen No. 1, (a) Constitutive Parameter Set No. 8, (b) $\bar{\sigma}$ — $\bar{\epsilon}$ comparison.

returning to Specimen No. 1 (Figure 18). This final simulation showed agreement comparable to that obtained prior to the change to Specimen No. 2 (from Specimen No. 1) made after the fifth simulation in the series of ten total simulations. The computationally predicted deformations at specimen failure are shown in Figure 19 for Simulations No. 9 and 10.

The constitutive parameter iteration sequence is shown in Figure 20, in the form of current and modified $\sigma - \epsilon$ curves for each constitutive parameter iteration. For the low aspect ratio specimen geometry, the iteration trend generally reduced the magnitude and scope of the changes that were made to the stress and strain values. This was followed by the change to the higher aspect ratio specimen geometry. The process repeated itself, culminating in the constitutive solution curve confirmed by both specimen geometries considered.

The initial power law extrapolation curve (Constitutive Parameter Set No. 1) and the solution curve (Constitutive Parameter Set No. 8) are plotted for comparison in Figure 21. The differences between the two curves were particularly significant in light of the effect which they have on the global specimen response through the neck deformation and localization process. The solution curve was clearly not predictable a priori from examination of the experimental data from the specimens alone. This indicates that significant inhomogeneity was present at even moderate engineering strains, consistent with earlier studies cited above. The solution parameter values are also given in Table 1.

The continuum material toughness for the material deformation histories predicted by the constitutive solution parameters may be defined as the critical strain energy density per unit mass, i.e.

$$w_c = \int_0^{(\epsilon_{ij})_c} \frac{\sigma_{ij}}{\rho} d\epsilon_{ij}. \quad (17)$$

Here, ρ is the mass density and $(\epsilon_{ij})_c$ is the strain state at fracture of the point. In the case of material deformation for which the volume change is not significant, the critical energy density per unit volume is equally appropriate, i.e.

$$w_c = \int_0^{(\epsilon_{ij})_c} \sigma_{ij} d\epsilon_{ij}. \quad (18)$$

The energy density per unit volume definition will be used for HSLA-80 steel. The use of an energy density criterion of material damage and failure is consistent with the ideas of Freudenthal (1950) and Gillemot (1976).

The maximum strain energy density value occurred at the center of each specimen. The integration of stress components over corresponding strain components, as obtained from the computational simulations for the specimen deformation range determined by experiment, produced critical strain energy density values of $1.39 \times 10^9 \text{ N-m/m}^3$ ($2.02 \times 10^5 \text{ lb-in/in}^3$) from Specimen No. 1 and $1.35 \times 10^9 \text{ N-m/m}^3$ ($1.96 \times 10^5 \text{ lb-in/in}^3$) from Specimen No. 2. Dissipative micromechanisms, being sensitive to deformation history, influence the critical value. Multiaxial stress-strain component histories are present from the onset of deformation in Specimen No. 1 due to its low gage section aspect ratio. This suggests that the critical energy density value obtained from Specimen No. 1 is relevant for the prediction of fracture ahead of macroscopic defects. This issue has been discussed by Gensheimer, Kirby and Jolles (1988) for HY-100 steel constitutive behavior and compact fracture specimen crack initiation.

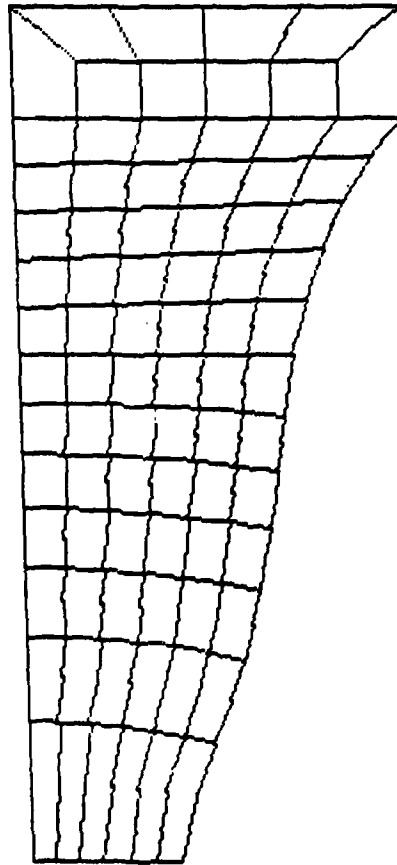


Figure 19 — Computationally predicted specimen deformation at failure using solution curve (Constitutive Iteration No. 8), (a) Computational Simulation No. 10 using Specimen 1, (b) Computational Simulation No. 9 using Specimen No. 2.

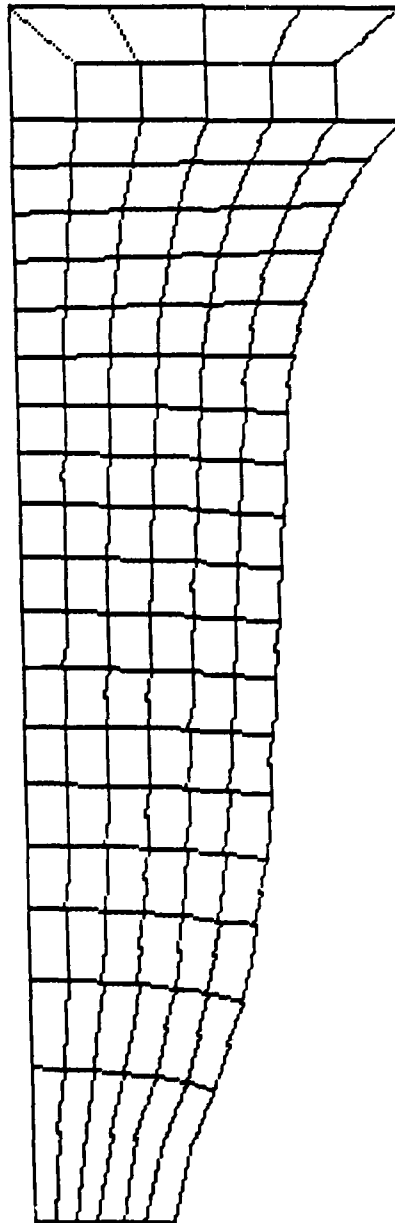


Figure 19 (Continued) — Computationally predicted specimen deformation at failure using solution curve (Constitutive Iteration No. 8), (a) Computational Simulation No. 10 using Specimen 1, (b) Computational Simulation No. 9 using Specimen No. 2.

CONSTITUTIVE PARAMETER INTERATION	SPECIMEN GEOMETRY	
	$L_0/D_0 = 1.0$	$L_0/D_0 = 2.0$
1		
2		
3		
4		
5		
6		
7		
8		
9		
10		

Figure 20—Summary of constitutive parameter specimen iteration sequence.

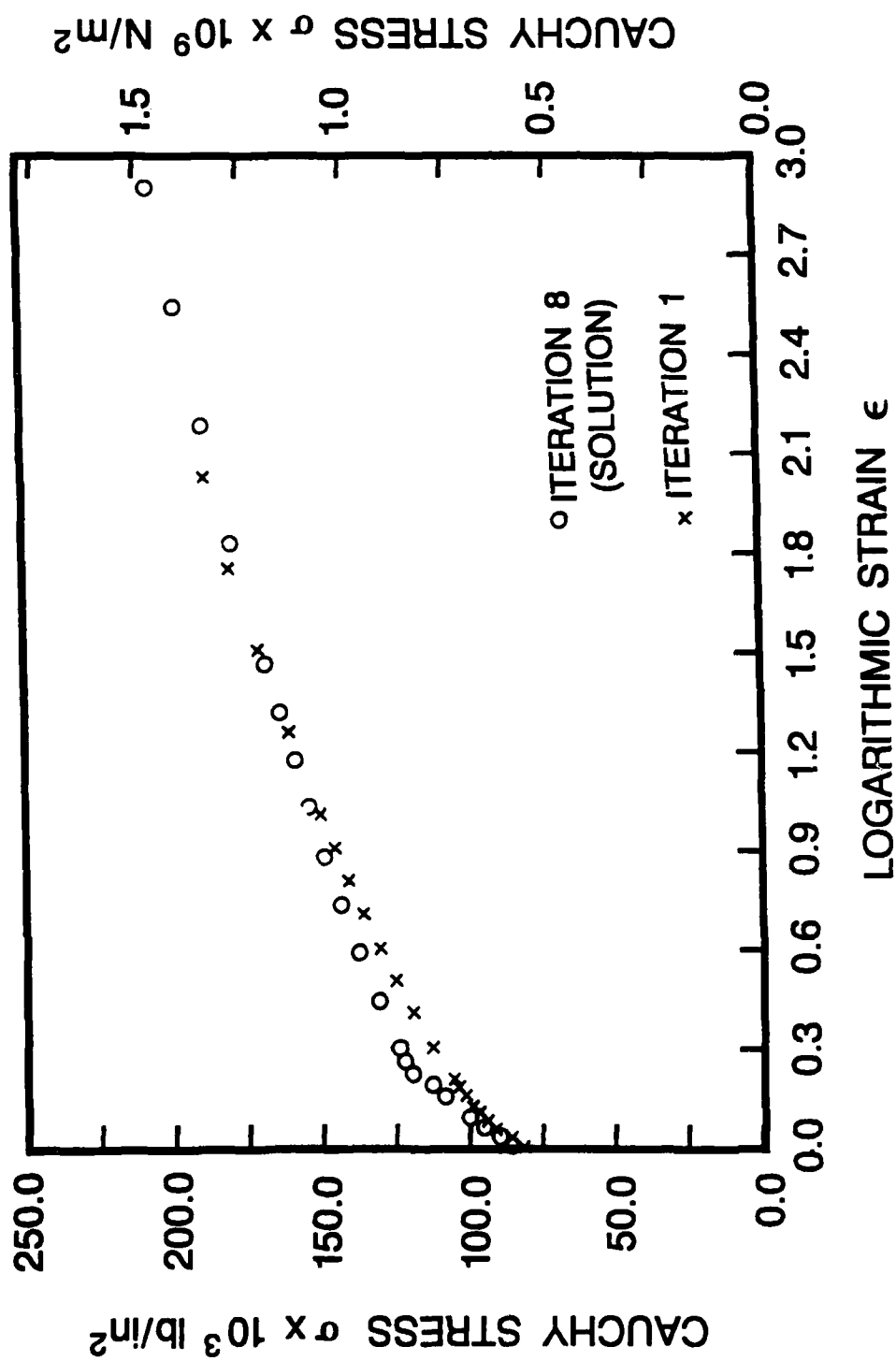


Figure 21—Initial constitutive parameters from power law extrapolation curve (Constitutive Iteration No. 1) and solution curve (Constitutive Iteration No. 8).

Table 1 — Constitutive solution for HSLA-80 steel

Uniaxial Cauchy Stress		Log Plastic Strain
$\sigma \times 10^8 \text{ N/m}^2$	$(\sigma \times 10^3 \text{ lb/in}^2)$	ϵ^p
5.93	(86.0)	0.0000
6.21	(90.0)	0.0275
6.58	(95.5)	0.0550
6.94	(100.6)	0.0825
7.51	(108.9)	0.145
7.77	(112.8)	0.182
8.27	(120.0)	0.218
8.41	(122.1)	0.254
8.56	(124.1)	0.290
9.06	(131.4)	0.436
9.51	(137.9)	0.580
9.92	(143.8)	0.726
10.30	(149.4)	0.871
10.66	(154.6)	1.016
11.00	(159.6)	1.161
11.33	(164.4)	1.307
11.65	(169.0)	1.452
12.40	(179.9)	1.763
13.10	(190.0)	2.178
13.76	(199.6)	2.542
14.40	(208.8)	2.904

Elastic modulus, $E = 2.06 \times 10^{11} \text{ N/m}^2$ ($30.0 \times 10^6 \text{ lb/in}^2$)

Poisson ratio, $\nu = 0.3$

SUMMARY

Accurate constitutive parameter values are necessary to describe the full range of large strain, inelastic deformation exhibited by polycrystalline metal alloys. Direct measurement of these parameters is generally not possible for most ductile metal alloys of interest. Deformation inhomogeneity makes the determination of material constitutive parameters at large strains nontrivial. Iterative solution for these parameters is a practical method for their determination.

In this investigation, the iterative solution for HSLA-80 steel constitutive parameters is accomplished through the combined use of multiple tensile specimen geometries, digital video image processing, nonlinear finite element simulation and software which compares successive computational simulations to laboratory data. Video recording and image processing are used to store the image, determine the deformed specimen profile and quantify data for comparison to computation. Nonlinear finite element simulations of the specimens are used to effectively treat the material constitutive parameters as the unknowns. The comparison software was developed to interpret the experimental data and computational data for direct comparison. Global load versus displacement responses and surface deformations within the specimen gage length, being measurable and observable quantities, are compared in order to identify the computationally predicted, but not directly observable, constitutive parameters which are responsible for the onset of predicted deformation errors. With this assessment of candidate constitutive parameters, corrected parameters are developed for subsequent iteration. This process is repeated until the solution constitutive parameters for the HSLA-80 material are inferred from observable response correlation. Correlation across two specimen geometries was employed in the laboratory experiments and computational simulations to facilitate iteration and ensure constitutive parameter geometry independence.

The utility of this approach lies in its ability to assess continuum material response which is not directly observable by conventional methods of laboratory data reduction and to facilitate rapid convergence to the solution parameters. In addition, these techniques can be used to examine the validity of a proposed constitutive formulation by examining the validity of constitutive parameters which satisfy the formulation. Finally, the approach discussed in this investigation is prerequisite to material characterization strategies whose solution include both the constitutive formulation and solution parameters.

REFERENCES

- ASTM 1984a, "Shear Modulus at Room Temperature, E143-61", *Annual Book of ASTM Standards, Section 3*, ASTM, Philadelphia, PA, pp. 315-319.
- ASTM, 1984b, "Tension Testing of Metallic Materials, E8-83", *Annual Book of ASTM Standards, Section 3*, ASTM, Philadelphia, pp. 130-150.
- Bridgman, P.W., 1952, *Studies in Large Plastic Flow and Fracture*, New York, McGraw-Hill.
- Chen, W., 1971, "Necking of a Bar," *J. Mech. Phys. Solids*, Vol. 20, pp. 111-127.
- Chen, L.G., 1983, "Necking in Uniaxial Tension," *Int. J. Mech. Sci.*, Vol. 25, pp. 47-57.
- Freudenthal, A.M., 1950, *The Inelastic Behavior of Engineering Materials and Structures*, Wiley, New York.

- Gensheimer, V.M., Kirby G.C. III and Jolles, M. I., "Analytical Prediction of Fracture Toughness in a Compact Specimen," *Engng. Fract. Mech.* (In review).
- Ghosh, A.K., 1974, "Strain Localization in the Diffuse Neck of Sheet Metal," *Metall. Trans.*, Vol. 5, pp. 1607-1616.
- Ghosh, A.K., 1977, "Tensile Instability and Necking in Materials with Strain Hardening and Strain Rate Hardening," *Acta Metall.*, Vol. 25, pp. 1413-1424.
- Gillemot, L.F., 1976, "Criterion of Crack Initiation and Spreading", *Engng. Fract. Mech.*, Vol. 8, pp. 239-253.
- G'Sell, C., Aly-Helal, N.A. and Jonas, J.J., 1983, "Effect of Stress Triality on Neck Propagation During the Tensile Stretching of Solid Polymers," *J. Mat. Sci.*, Vol. 18, pp. 1731-1742.
- G'Sell, C. and Jonas, J.J., 1979, "Determination of the Plastic Behavior of Solid Polymers at Constant True Strain Rate," *J. Mat. Sci.*, Vol. 14, pp. 583-591.
- Hart, E.W., 1967, "Theory of the Tensile Test," *Acta Metall.*, Vol. 15, pp. 351-355.
- Hartley, K.A., Duffy, J. and Hawley, R.H., 1987, "Measurement of the Temperature Profile During Shear Band Deformation in Steels Deforming at High Strain Rates," *J. Mech. Phys. Solids*, Vol. 35, No. 3, pp. 283-301.
- Hibbitt, H.D., Karlsson, B.I. and Sorensen, E.P., 1984a, *ABAQUS Theory Manual*, Hibbitt, Karlsson and Sorensen, Inc., Providence, RI.
- Hibbitt, H.D., Karlsson, B.I. and Sorensen, E.P., 1984b, *ABAQUS User's Manual*, Hibbitt, Karlsson and Sorensen, Inc., Providence, RI.
- Hutchinson, J.W., 1979, "Survey of Some Recent Works on the Mechanics of Necking," *Proc. 8th U.S. Nat. Congr. of Appl. Mech.*, North Hollywood, West Point, pp. 87-98.
- Hutchinson, J.W. and Neale, K.W., 1983, "Neck Propagation," *J. Mech. Phys. Solids*, Vol. 31, pp. 405-426.
- Iding, R.H., Pister, K.S. and Taylor, R.L., 1974, "Identification of Nonlinear Elastic Solids by a Finite Element Method," *Comp. Meth. Appl. Mech. Engng.*, Vol. 4, pp 121-142.
- Jonas, J.J. and Baudalet, B., 1977, "Effect of Crack and Cavity Generation on Tensile Stability," *Acta Metall.*, Vol. 25, pp. 43-50.
- Jonas, J.J., Holt, R.A. and Coleman, C.E., 1976, "Plastic Stability in Tension and Compression," *Acta Metall.*, Vol. 24, pp. 911-918.
- Kachanov, L.M., 1986, *Introduction to Continuum Damage Mechanics*, Martinus Nijhoff, Boston.
- Kleiber, M., 1986, "On Plastic Localization and Failure in Plane Strain and Round Void Containing Bars," *Int. J. Plasticity*, Vol. 2, pp. 205-221.

- Klepaczko, J.R. and Chiem, C.Y., 1986, "On Rate Sensitivity of f.c.c. Metals, Instantaneous Rate Sensitivity and Rate Sensitivity of Strain Hardening," *J. Mech. Phys. Solids*, Vol. 34, No. 1, pp. 29-54.
- Kocks, U.F., Jonas, J.J. and Macking, H., 1979, "The Development of Strain Rate Gradients," *Acta Metall.*, Vol. 27, pp. 419-432.
- Korbel, A., Raghunathan, V.S., Teirlinck, D., Sptizig, W., Richmond, O. and Embury, J.D., 1984, "A Structural Study of the Influence of Pressure on Shear Band Deformation," *Acta Metall.*, Vol. 32, No. 4, pp. 511-519.
- Krajcinovic, D., 1984, "Continuum Damage Mechanics," *Appl. Mech. Rev.*, Vol. 37, No. 1, pp. 1-6.
- Krempl, E. and Lu, H., "The Hardening and Rate-Dependent Behavior of Fully Annealed AISI Tupe 304 Stainless Steel Under Biaxial In-Phase and Out-of-Phase Strain Cycling at Room Temperature," *J. Engng. Mat. Tech.*, Vol. 106, No. 4, pp. 376-382.
- Lian, J. and Baudalet, B., 1986, "Necking Development and Strain to Fracture under Uniaxial Tension," *Mat. Sci. Engng.*, Vol. 84, pp. 157-162.
- Lin, I.-H., Hirth, J.P. and Hart, E.W., 1981, "Plastic Instability in Uniaxial Tension Tests," *Acta Metall.*, Vol. 29, pp. 819-827.
- Matic, P., 1985, "Numerically Predicting Ductile Material Behavior from Tensile Specimen Response," *Th Appl. Fract. Mech.*, Vol. 4, pp 13-28.
- Matic, P., Kirby, G.C. III, Jolles, M.I., 1988, "The Relationship of Tensile Specimen Size and Geometry Effects to Unique Constitutive Parameters for Ductile Materials," *Proc. Roy. Soc. London* (In press).
- McDowell, D. L., "An Evaluation of Recent Developments in Hardening and Flow Rules for Rate-Independent, Nonproportional Cyclic Plasticity," *J. Appl. Mech.*, Vol. 54, No. 2, pp 323-334.
- Naghdi, P.M. and Nikkel, D.J. Jr., 1986, "Two Dimensional Strain Cycling Necking and Failure in Porous Plastic Solids," *J. Appl. Mech.*, Vol. 53, pp. 821-830.
- Needleman, A., 1972, "A Numerical Study of Necking in Circular Cylindrical Bars," *J. Mech. Phys. Solids*, Vol. 20, pp. 111-127.
- Needleman, A. and Becker, R., 1986, "Effect of Yield Surface Curvature on Necking and Failure in Porous Plastic Solids," *J. Mech. Phys. Solids*, Vol. 53, pp. 491-498.
- Norris, D.M., Moran, B., Scudder, J.K. and Quinones, D.F., 1978, "A Computer Simulation of the Tension Test," *J. Mech. Phys. Solids*, Vol. 26, pp. 1-19.
- Perzyna, P., 1984, "Constitutive Modeling of Dissipative Solids for Postcritical Behavior and Fracture," *J. Engng. Mat. Tech.*, Vol. 106, pp. 410,419.
- Pister, K.S., 1974, "Constitutive Modeling and Numerical Solution of Field Problems," *Nuc. Engng. Design*, Vol. 28, pp 137-146.

- Semiatin, S.L., Ghosh, A.K. and Jonas, J.J., 1985, "A Simplified Numerical Analysis of the Sheet Tensile Test," *Metall. Trans.*, Vol. 16A, pp. 2291-2298.
- Semiatin, S.L., Staker, M.R. and Jonas, J.J., 1984, "Plastic Instability and Flow Localization in Shear at High Rates of Deformation," *Acta Metall.*, Vol. 32, No. 9, pp. 1347-1354.
- Triantafyllidis, N., Needleman, A. and Tvergaard, V., 1982, "on the Development of Shear Bands in Pure Bending," *Int. J. Solids Structures*, Vol. 18, No. 2, pp. 121-138.
- Tvergaard, V., 1987, "The Effect of Yield Surface Curvature and Void Nucleation on Plastic Flow Localization," *J. Mech. Phys. Solids*, Vol. 35, No. 1, pp. 43-60.
- Tvergaard, V. and Needleman, A., 1984, "Analysis of the Cup-Cone Fracture in a Round Tensile Bar," *Acta Metall.*, Vol. 32, pp. 157-169.
- Tvergaard, V., Needleman, A. and Lo, K.K., 1981, "Flow Localization in the Plane Strain Tensile Test," *J. Mech. Phys. Solids*, Vol. 29, No. 2, pp. 115-142.

APPENDIX I

Laboratory Specimen Imperfections

Prior to testing, the tensile specimen gage section diameters were measured. Deviations from the nominal specimen gage diameter D_0 were tabulated below for each specimen as the maximum and minimum specimen diameters, $(D_0)_{\max}$ and $(D_0)_{\min}$ measured along the gage length. The diameter imperfection for each specimen was defined as

$$d_0 = \frac{(D_0)_{\max} - (D_0)_{\min}}{(D_0)_{\max} + (D_0)_{\min}} \quad (\text{AI.1})$$

This may be interpreted as the average deviation (from the average diameter) divided by the average diameter. The diameter imperfection values are tabulated in Table AI.1 The specimens modeled for the computational simulations were assumed to be free of any geometric imperfections.

Table AI.1 — Laboratory Tensile Specimen Diameter Imperfection

Specimen Geometry	Nominal Gage Length	Nominal Gage Diameter	Diameter Imperfection
1	1.27 cm	1.275 cm	0.0088 0.0118 0.0059 0.0059 0.0089
2	2.54	1.275	0.0040 0.0059 0.0049 0.0040 0.0030
3	3.81	1.275	0.0088 0.0109 0.0109 0.0111 0.0089
4	5.08	1.275	0.0385 0.0394 0.0467 0.0348 0.0308

APPENDIX II

Specimen Neck Eccentricity Values

Specimen neck eccentricity serves as a measure of deformation symmetry. It is defined as

$$e = \left| 1 - \frac{2z_n}{L} \right| \quad (\text{AII.1})$$

where e is the neck eccentricity at specimen fracture, z_n is the distance of the neck plane from end of specimen gage length and L is the gage length at specimen fracture. For the L_0/D_0 ratios considered in this investigation, only symmetric deformation is computationally predicted. This is confirmed by the low eccentricity values, tabulated below, which were calculated from the final deformed shape of each laboratory specimen. (Broken deformation symmetry, in the form of neck location asymmetry, was predicted and observed for HY-100 specimens when specimen L_0/D_0 ratios exceeded 4.0. This effect is apparently sensitive to the material behavior, and can be used as an additional test of constitutive solution parameter. For this investigation of HSLA-80, only symmetric necking was experimentally observed and computationally predicted for the specimen geometries considered.)

Table AII.1 — Laboratory Specimen Neck Location Eccentricity

Specimen Type	Neck Eccentricity
1	0.0909
	0.0788
	0.0109
	0.0539
	0.0012
2	0.0520
	0.1046
	0.0163
	0.0142
	0.1676
3	0.0088
	0.0109
	0.0109
	0.0111
	0.0089
4	0.0385
	0.0394
	0.0467
	0.0348
	0.0308